



Ben-Gurion University of the Negev
Faculty of Engineering Sciences
Department of Mechanical Engineering

**INVESTIGATION OF NATURAL
CONVECTION IN POROUS MEDIUM
BY IMMERSED BOUNDARY
METHOD**

By: Shahar Idan

October 2016



Ben-Gurion University of the Negev
Faculty of Engineering Sciences
Department of Mechanical Engineering

Investigation of natural convection in porous medium by immersed boundary method

By: Shahar Idan

Under the supervision of Dr. Yuri Feldman

Chairman of the
teaching committee
signature:

Professor Oren Sadot

Supervisor signature:

Dr. Yuri Feldman

Feldman

אוקטובר 2016

תשרי התשע"ו

Acknowledgment

I would like to dedicate this study to my wife, Natalie, who supported me every step of the way, to my family who were there for me since day one and to my supervisor, Dr. Yuri Feldman, whose hard work around the clock made this study possible.

"The true sign of intelligence is not knowledge but imagination". Albert Einstein.

Abstract

Today, a considerable amount of energy is required to maintain a comfortable indoor climate in residential and office buildings, as well as in public shopping centers. Efficient optimization of the thermal insulation properties of hollow blocks, widely used as building elements of ventilated facades and masonry structures, is an important step in the direction of enhancing indoor climate control.

The goal of the present study is to develop a generalized method for the design of "smart" passive thermo-insulating materials based on statistical evaluation of the confined natural convection flow in the presence of heterogeneous porous media. Confined natural convection flow developing inside a differentially heated cavity (comprising a convenient model for the air-filled cavity in the mid-core of a hollow construction block) is chosen as a computational testbed.

The heterogeneous porous media are modelled by unconnected packed beds of equi- and non-equi-sized cylinders. Each cylinder is intelligently placed in the bulk of the natural convection flow to efficiently suppress the momentum at the most energetic regions of the flow. The spatial location of each cylinder is obtained by applying linear stability analysis to the 2D natural convection flow in the presence of the modelled porous media. The flow is treated by the mesoscale approach, implicitly resolving the flow fields in the vicinity of the immersed cylinders by the immersed boundary (IB) method (IBM). The results obtained for 2D configurations were extensively validated for realistic 3D flows.

Basic statistical evaluation of the generated porous media patterns is performed to generalize the developed method for the design of "smart" thermo-insulating materials. It is shown that the efficiency of the thermal insulation of the porous media is closely related to the diameter of the cylinders modelling it. The study comprises an

important milestone in the design and manufacturing of “smart” thermo-insulating materials from available off-the-shelf porous materials.

Table of Contents

Chapter 1: Introduction and Literature Survey	1
1.1 Motivation of the study	1
1.1.1 Natural convection inside a differentially heated cavity	2
1.1.2 “Smart” passive thermo-insulating materials.....	4
1.2 Objectives of the study	7
Chapter 2: Theoretical Background.....	9
2.1 Chapter overview	9
2.2 3D incompressible natural convection flow	9
2.2.1 Physical model.....	10
2.2.2 Space and time discretization	11
2.3 “Smart” thermal insulation – concept.....	13
2.3.1 Immersed boundary (IB) method	13
2.3.2 Fully pressure-velocity coupled direct (FPCD).	17
Immersed boundary augmentation	18
2.3.3 Steady state immersed boundary FPCD solver	21
2.3.4 Linear stability immersed boundary FPCD solver.....	23
2.3.5 Direct forcing approach	26
Chapter 3: Results and Discussion.....	29
3.1 Chapter overview	29
3.2 “Smart” thermal-insulation	30
3.2.1 2D differentially heated cavity with 8:1 aspect ratio	32
3.2.2 Generalized “smart” thermo-insulator in a cubical differentially heated cavity..	37
3.2.3 Insulating properties and 3D validation of equi-sized patterns.....	48
Chapter 4: Summary and Conclusions.....	57
Appendix A: De Casteljau Bézier curve	59
Appendix B: Estimation of dimensions of realistic hollow construction blocks	65
Appendix C: Deriving the dimensionless equations of motion	67
References.....	71

Nomenclature

Initials

<i>A</i>	Optimization criterion parameter	
<i>B</i>	An arbitrary immersed object	
<i>B</i>	Linear stability diagonal matrix	
<i>D_o</i>	Computational domain (IB related)	
<i>D</i>	Cylinder diameter (non-dimensional)	
<i>f</i>	Discrete volumetric force on the Eulerian grid	
<i>F</i>	Volumetric boundary forces (non-dimensional)	
<i>g</i>	Gravitational acceleration	[m/s^2]
<i>H</i>	Helmholtz operator	
<i>I</i>	Interpolation operator (IB related)	
<i>I</i>	Identity operator	
<i>J</i>	Jacobian matrix	
<i>K</i>	Smoothing value	
<i>L</i>	Characteristic length (non-dimensional)	
<i>N</i>	Number of points belonging to the vertical boundary	
<i>Nu</i>	Nusselt number	
<i>p, P</i>	Pressure (non-dimensional)	
<i>q</i>	Eulerian heat source (non-dimensional)	
<i>Q</i>	Lagrangian point's heat fluxes (non-dimensional)	
<i>r</i>	Distance (non-dimensional)	
<i>R</i>	Regularization operator (IB related)	
<i>Ra</i>	Rayleigh number	
<i>Re</i>	Reynolds number	
<i>S</i>	Corresponding to all the cells belonging to the surface of immersed body	
<i>t</i>	Time (non-dimensional)	
<i>T</i>	Temperature	[°K]
ΔT	Temperature difference	[°K]
<i>U</i>	Value of the boundary velocity (non-dimensional)	

\mathbf{u}	Velocity vector field (non-dimensional)
\mathbf{X}	Lagrangian position vector (non-dimensional)
\mathbf{x}	Eulerian position vector (non-dimensional)

Superscript

n	Time step index
\sim	Perturbations
$*$	Intermediate predicted velocity field
Γ	Value on body's boundary
$\bar{}$	Averaged

Subscript

b	Body related
cyl	Cylinder related
i,j	Indices of computational domain points
k	Index of Lagrangian points
p	Pressure component
H	Temperature hot
C	Temperature cold
cr	Critical values
u	Velocity in the x direction component
v	Velocity in the y direction component
w	Velocity in the z direction component
x	x direction component
y	y direction component
z	z direction component

Greek symbols

α	Thermal diffusivity	$[m^2/sec]$
β	Adiabatic coefficient of thermal expansion	$[1/^\circ K]$
δ	Discrete delta function	
ζ_k	Z coordinate of the Lagrangian point	
θ	Temperature (non-dimensional)	
Θ	Temperature at the Lagrangian points (non-dimensional)	
λ	Leading eigenvalue	
μ	Dominant eigenvalue, can be related to the leading eigenvalue λ	
ν	Kinematic viscosity	$[m^2/sec]$
ξ_k	X coordinate of the Lagrangian point	
ρ	Mass density	$[kg/m^3]$
ω	Real part of the eigenvalue	
ϕ	Porosity	
ψ_k	Y coordinate of the Lagrangian point	
σ	Angular frequency / standard deviation	
Ω	Corresponds to a group of flow cells located in the close vicinity of the surface of the immersed body	

List of figures

Number	Description	Page
1.1	Typical hollow blocks: (a) Cement building block partitioned into 2 equal parts of air filled cavities, (b) Red clay building block partitioned into 40 equal parts of air filled cavities.....	1
1.2	Cross section of a partitioned building block with boundaries held at constant temperatures T_H and T_C (hot and cold, respectively).....	3
1.3	Methods for decreasing convective heat transfer in differentially heated cavity: (a) Filled with equally spaced conducting solid blocks [23], (b) Protuberances inserted into the bulk of the flow [11]	4
1.4	A typical flow field inside a differentially heated cavity filled with thermal insulating material for $Ra = 10^7$: (a) $\phi = 0.9$, (b) $\phi = 0.8$, (c) $\phi = 0.7$, (d) $Nu - Ra$ functionality for a differentially heated cavity filled with thermal insulating material, each trend represents different porosity [33]	6
1.5	Physical model of the hollow block with implants of “smart” porous media insulators: (a) General exploded view, (b) Cross section view determining 2D model of differentially heated cavity.....	7
2.1	Physical model and system of coordinates for the differentially heated cavity. Colors correspond to the temperature distribution at the mid cross section typical of the steady state flow.....	11
2.2	A schematic staggered grid discretization of a 2D computational domain D_o , with a slice of IB formulation for a body, B . The virtual shell, whose thickness is equal to the grid cell width, is shaded to distinguish it from the rest of the grid. The horizontal and vertical arrows (\rightarrow, \uparrow) represent the discrete velocity locations, u_i and v_i , respectively. The pressure p_j and the temperature T_j are applied at the center of each grid cell and designated by (\times). Lagrangian points $\mathbf{X}_k = (\xi_k, \psi_k)$ along ∂B are shown as black dots (\cdot) where volumetric boundary forces $\mathbf{F}_k = (\mathbf{F}_{kx}, \mathbf{F}_{ky})$ and volumetric boundary heat fluxes, Q_k , are applied [33].....	15
3.1	Contours of criterion \mathbf{A} and the corresponding steady state distribution of temperature, θ , with superimposed streamlines obtained at $Ra = 2.15 \times 10^6$ for no obstacles.....	31

3.2	Evolutionary stages of the process of generation of implants of “smart” thermal insulators for a differentially heated cavity of aspect ratio 8:1: (top) A criterion, (bottom) the corresponding temperature distribution.....	33
3.3	Value of the averaged \overline{Nu} number obtained for the vertical hot wall of the cavity at $Ra_{cr} = 3.32 \times 10^5$ and the critical Rayleigh number, Ra_{cr} , for the steady-unsteady transition obtained by linear stability analysis as a function of number of cylindrical obstacles for a grid of 800x100.....	37
3.4	Successive representative stages of building a pattern of “smart” insulators characterized by the minimal porosity value, $\phi = 0.51$. The final pattern of the porous material is confined by the black solid line. The colors correspond to the distribution of the control parameter \mathbf{A}	39
3.5	Successive representative stages of building a pattern of “smart” insulators characterized by the minimal porosity value, $\phi = 0.64$. The final pattern of the porous material is confined by the black solid line. The colors correspond to the distribution of the control parameter \mathbf{A}	40
3.6	Temperature distribution with superimposed streamlines for: (a) Configuration without porous implants, (b) Configuration with porous implants characterized by $\phi = 0.51$, (c) Configuration with porous implants characterized by $\phi = 0.64$	41
3.7	Efficiency characteristics of the porous media implants characterized by the minimal ($\phi = 0.51$) and the maximal ($\phi = 0.64$) values of porosity, ϕ , in terms of: (a) \overline{Nu} number, averaged over vertical (hot or cold) boundaries, (b) Critical Ra_{cr} number at which the transition from steady to unsteady flow takes place via Hopf bifurcation.....	41
3.8	Averaged confining contour created using the heterogeneous patterns described above and the coordinate locations representing the center of the contour.....	42
3.9	Two configurations characterized by approximately the same porosity, $\phi \approx 0.59$, and different thermal insulating capacities: (a) $\overline{Nu}=6.3393$, (b) $\overline{Nu}=3.9832$. All the results are obtained for $Ra = 2.15 \times 10^6$	48
3.10	Distribution of optimization parameter \mathbf{A} and the corresponding temperature field with superimposed streamlines obtained for the implants characterized by approximately the same porosity, $\phi \approx 0.59$, for 2D flow. The implants contain in total: (a) 94 cylinders. (b) 42 cylinders, (c) 28 cylinders, (d) 16 cylinders, (e) 6 cylinders.....	50

3.11	Distribution of temperature field in the mid cross section of 3D cavity obtained for the implants characterized by approximately the same porosity, $\phi \approx 0.59$, for 3D flow. The implants contain in total: (a) 94 cylinders, (b) 42 cylinders, (c) 28 cylinders, (d) 16 cylinders, (e) 6 cylinders.....	52
A.1	Smoothing edged polygon using De Casteljaou Bézier method.....	57
A.2	Q_0 is a convex combination of P_0 and P_1 depending on the parameter t , example of a case where $t=1/3$ [49].....	57
A.3	(a) Example of an arc where $t=1/2$, (b) Illustration of how the points Q_0, Q_1 and R_0 advance as t increases from 0 to 1 where R_0 draws the curve, [49] and [50].....	58
A.4	Cubic Bézier: (a) s_0 defines the curve using the anchors and the control points, (b) The effects of the control points on the curve [49].....	60
A.5	Steps used by Maxim [51] in order to find the optimal control points which will best represent the polygon.....	61
A.6	From left to right, Bezier made with 0.5 smoothing value and 0.3 smoothing value.....	62
B.1	Cross section of a hollowed block ($W \times H \times L$) with t as its wall thickness.....	64

List of tables

Number	Description	Page
1	Results obtained for the set of 10 different patterns in order of decreasing porosity, ϕ . The patterns are modelled by unconnected packed beds of cylinders of varying diameters, drawn in accordance with the Gaussian distribution characterized by an average value of $D_{av} = 0.1$ and standard deviation of $\sigma = \pm 0.02$	43
2	Results for chosen patterns from the 2D sets with approximately the same porosity, $\phi \approx 0.59$, for $Ra = 2.15 \times 10^6$	48
3	Results for 3D simulations for $Ra = 2.15 \times 10^6$ with Richardson's extrapolation.....	53
4	\overline{Nu} values obtained for the opposite temperature gradient for the representative 2D and 3D configurations and the deviations in \overline{Nu} values obtained for the corresponding configurations with “direct” temperature gradient.....	54

Chapter 1: Introduction and Literature Survey

1.1 Motivation of the study

The rapid growth in energy consumption required for heating and cooling residential buildings and offices (presently accounting for more than one third of the total energy budget in the European Community [1]) stimulates the promotion of energy saving technologies when building and maintaining the premises [2]. Efficient optimization of the thermal and insulation properties of hollow blocks, widely used as the building elements of ventilated facades [3] and masonry structures [4], is an important step in this direction, enabling the enhancement of indoor climate control. The high popularity of hollow blocks is due to their light weight and high thermal and acoustic resistances, achieved due to a large air-filled cavity in the mid-core of the block. While partition of the air-filled cavity can vary significantly without compromising the strength of the block (typically between 2 and 8 equal parts and up to 100 parts for the coarse and dense partitioned configurations (see Fig. 1.1)), it has a substantial impact on the convective component of heat flux passing through the hollow construction block. This is because the internal walls of a partitioned cavity suppress the intensity of convective air circulation by two physical mechanisms: first, they enforce the non-slip (zero) velocities on the internal surfaces and second, they split the flow up and thus decrease the geometrical dimensions of the largest flow scales.

Unfortunately, simply partitioning the air-filled cavity by introducing many internal walls is far from an optimal solution to improving thermal insulation. In fact, reducing the convective heat flux in such a way is not only apparently counterbalanced (at least partially) by the accompanying conductive and radiative heat fluxes, but also incurs the disadvantages of significant increases in weight and construction costs. While

there is a broad consensus about minimizing the conductive and radiative heat fluxes by increasing the porosity of the brick material ([5], [6]) and by decreasing radiation emissivity of recesses and the external surfaces of hollow bricks ([7], [8]), an efficient minimization technique for convective heat flux is still sought. Therefore, in the framework of the present study the focus is only on natural convection flow and does not consider the conduction and radiation.

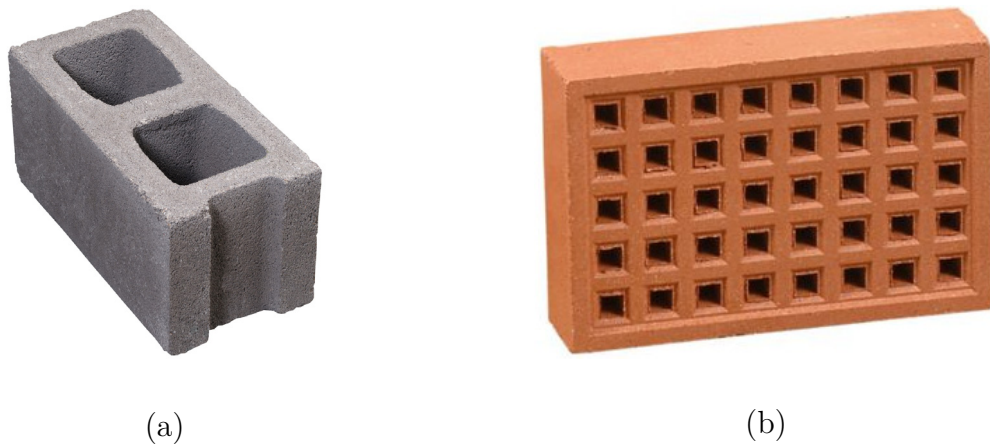


Figure 1.1: Typical hollow blocks: (a) Cement building block partitioned into 2 equal parts of air filled cavities, (b) Red clay building block partitioned into 40 equal parts of air filled cavities.

1.1.1 Natural convection inside a differentially heated cavity

Natural convection – the mechanism by which motion is generated in a fluid by density differences due to temperature gradients – is ubiquitous in our daily lives at a wide range of scales; these can vary from kilometers for open flows, such as atmospheric and oceanic circulations, to microns for confined configurations, such as blood and lymph flows inside human tissues. While moving, the fluid contributes to the exchange of thermal energy between the hot and the cold regions – a phenomenon known as convective heat transfer. The development of methods facilitating the efficient control of convective heat transfer has been the subject of intensive research in nuclear, civil, aerospace and mechanical engineering over the past few decades. Attention has been paid to decreasing convective heat transfer in a configuration known as a differentially

heated cavity, namely, a rectangular container in which one vertical wall is hot and the opposite vertical wall is cold, while all other walls are either insulated or perfectly conducting. This problem has become especially relevant in the past two decades as a result of the rapid growth in energy consumption for the heating and cooling of residential buildings and offices (presently accounting for more than one third of the total energy budget in the European Community [1]). As a result, new thermal design standards for the energy efficiency of residential buildings in hot summer/cold winter zones have recently been proposed [2]. A differentially heated cavity can be used as a convenient model for simulating the natural convection flow developing inside the double-skin facades and hollow bricks widely used in the modern building industry, (see Fig.1.2).

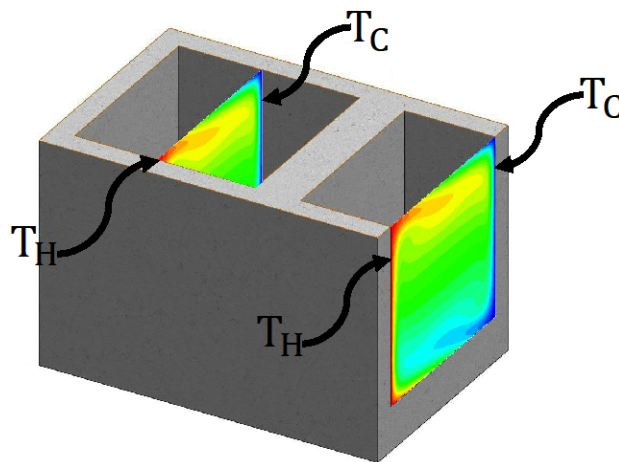


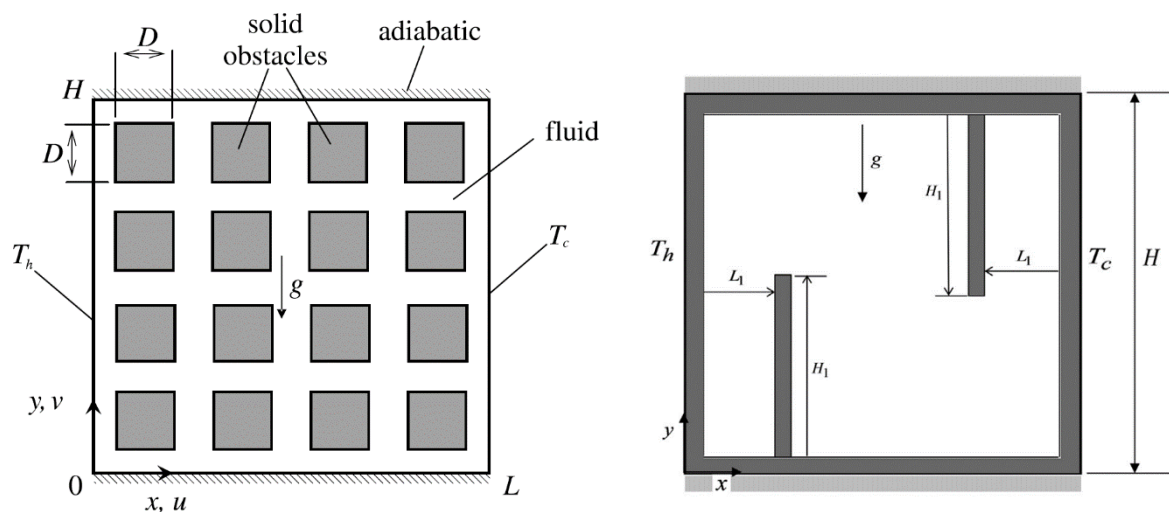
Figure 1.2: Cross section of a partitioned building block with boundaries held at constant temperatures T_H and T_C (hot and cold respectively).

To date, the majority of studies investigating ways to decrease heat flux in confined natural convection flows have been heuristic in character and based on breaking down the large scale convection cells. The pioneering works of Tong and Gerner [9] and Kangni et al. [10] were followed by a large number of studies which included various configurations and orientations of voids ([11], [12], [13], [14], [15], [16], [17], [18], [19]), insulating the boundaries of the voids ([20], [21]) and inserting flow obstacles ([22], [23], [24], [25], [26], [27], [28], [29]), to name a few. It is therefore necessary to develop a

formal generalized method that will facilitate intelligent control of heat flux in confined natural convection flows and will provide engineers with the tools to achieve optimized thermal insulation of buildings.

1.1.2 “Smart” passive thermo-insulating materials

Despite significant progress in decreasing convective heat flux in confined enclosures, the state of the art research in this area relies mostly on heuristic rather than on systematic methodology. The first attempt to reformulate the problem in terms of “smart” passive thermal insulation behavior is due to Costa [11]. It was demonstrated that protuberances inserted into the bulk of convective flow exhibit increasing self-adjusting inhibition of convection and radiation heat fluxes for higher temperature differences between the hottest and the coldest walls of the hollow construction block. Merrikh and Lage [23] studied the effect of equally spaced conducting solid square blocks on a differentially heated cavity with adiabatic horizontal boundaries using a continuum model, which treats the fluid and solid constituents individually. They tested the effect of the conductivity of the solid blocks and the effect of the number of solid blocks (a greater number of blocks requires smaller blocks) on the heat transfer across the enclosure for the Rayleigh numbers in the range of ($10^5 \leq Ra \leq 10^8$).

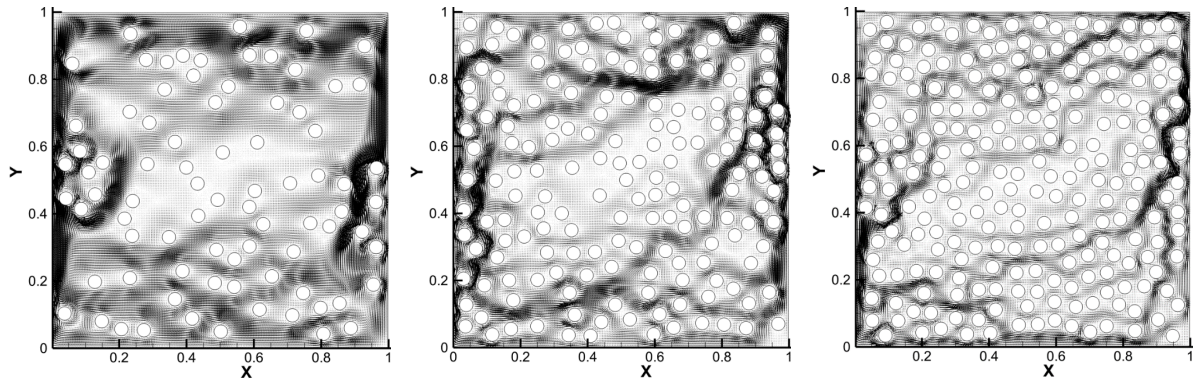


(a)

(b)

Figure 1.3: Methods for decreasing convective heat transfer in differentially heated cavity: (a) Filled with equally spaced conducting solid blocks [23], (b) Protuberances inserted into the bulk of the flow [11].

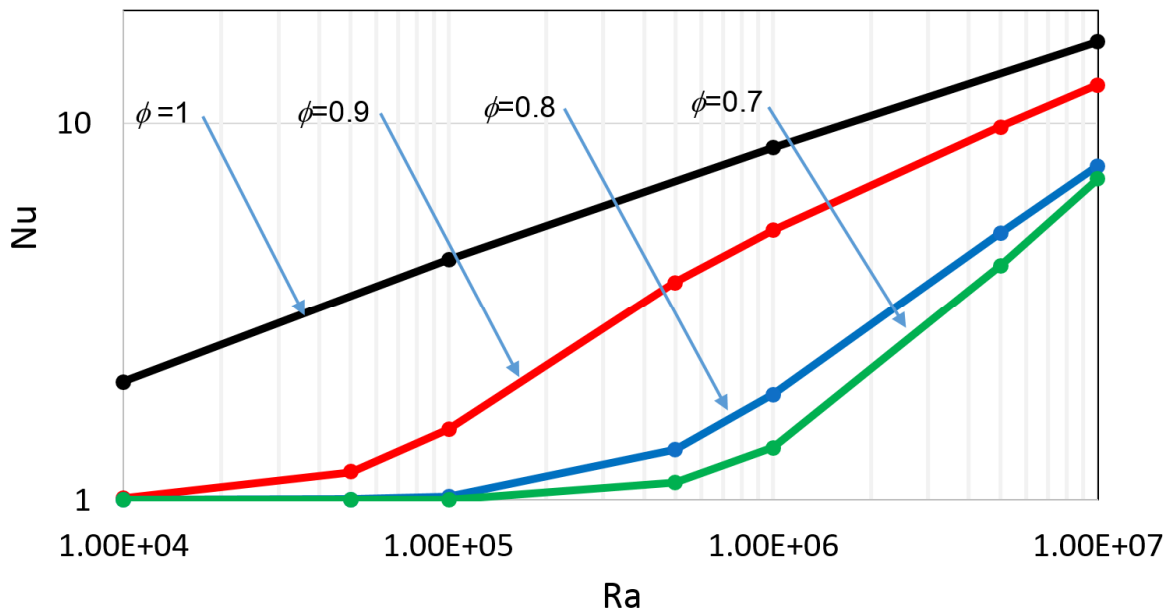
Afterwards, Braga and Lemos [30] compared the heat transfer characteristics across a square cavity filled with a fixed amount of conducting solid square and cylindrical obstacles. Some studies ([31] and [32], for example) use the volume-averaging macroscale approach to solve fluid flow equations. The present study utilizes a different – mesoscale – approach, explicitly resolving flow near the boundaries of the obstacles by enforcing non-slip kinematic constraints. This approach has gained popularity in the last decade due to the rapid development of computational power. Gulbeg [33] studied the insulating efficiency of heterogeneous porous media of varying porosities modelled by equi-sized cylinders randomly filling the differentially heated cavity, as shown in Figs. 1.3 a-c. As can be seen from Fig. 1.3d, at high Ra numbers there is no significant difference between the Nu values obtained for porosity values of $\phi = 0.8$ and $\phi = 0.7$, which clearly indicates that a random arrangement of porous media is not optimal. The next step towards deriving a formal methodology for intelligent control of the confined natural convection flow is to determine an optimization criterion that will define the location of the porous media. Gulbeg [33] tested two criteria. The first related to the perturbation of kinetic energy and the second to the perturbation of the temperature of the natural convection flow. It was found that optimizing with relation to the perturbation of kinetic energy criterion is significantly more efficient in decreasing the average value of the Nu number than with relation to the criterion comprising a perturbation of the temperature field.



(a)

(b)

(c)



(d)

Figure 1.4: A typical flow field inside a differentially heated cavity filled with thermal insulating material for $Ra = 10^7$: (a) $\phi = 0.9$, (b) $\phi = 0.8$ (c), $\phi = 0.7$, (d) $Nu - Ra$ functionality for a differentially heated cavity filled with thermal insulating material, each trend represents different porosity [33].

The most energetic regions where the flow oscillations are to be suppressed are determined by linear stability analysis in the presence of modelled porous media, as was recently established in the work of Gulbeg and Feldman [34]. The authors employed heterogeneous porous media modelled by unconnected packed beds of equi-sized circular cylinders, and reported a twofold decrease of the overall convective heat flux through the square differentially heated cavity when using optimally designed implants of porous media that occupy only 5% of the total volume.

1.2 Objectives of the study

The goal of the present work is to extend and generalize the concept of “smart” thermal insulators in the context of decreasing convective heat flux through the air-filled cavities in the mid-core of hollow construction blocks. The present study is divided into two parts. The first part of the study extends the results of Gulbeg and Feldman [35] by applying the methodology to the suppression of the most energetic regions of the confined natural convection flow that develop inside a differentially heated cavity of 8:1 vertical to horizontal aspect ratio. The second part of the present study focuses on the generation, statistical evaluation and validation of the recently established concept of “smart” thermal insulation for several sets of similar systems, utilizing square and cubical differentially heated cavities as computational testbeds.

Various implants of heterogeneous porous media modelled by sets (10 patterns in each set) of unconnected packed cylinders of non-uniform and uniform diameters were generated. Based on the obtained results, the shapes, spatial locations and porosity values of the modelled porous media which form implants are statistically evaluated. Each porous media implant embedded into the differentially heated cavity provides a twofold decrease in convective heat flux through the cavity boundaries. An emphasis is put on extensive validation of the established methodology for 3D realistic configurations obtained by extruding the porous media patterns obtained by the corresponding 2D analysis in the third direction, i.e. porous media will be modelled by arrays of 3D cylinders. A grid independence of all the obtained 3D results is established. It is also shown that the optimized hollow construction blocks operate with approximately the same insulation performance for both positive and negative temperature gradients across the block and can thereby benefit for both cooled and heated indoor environments.

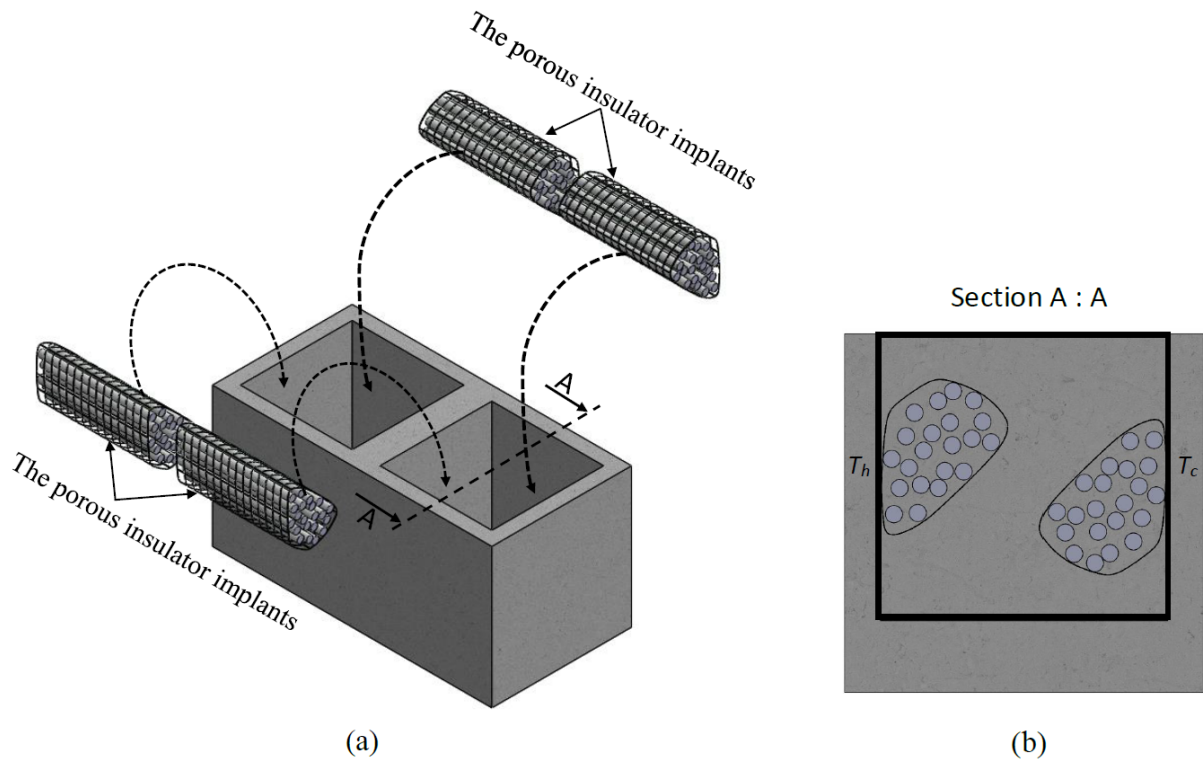


Figure 1.5: Physical model of the hollow block with implants of “smart” porous media insulator: (a) General exploded view, (b) Cross section view determining 2D model of differentially heated cavity.

Chapter 2: Theoretical Background.

2.1 Chapter overview

In this chapter, the physical model and numerical methodology utilized in the present study are presented. The first part of the study focuses on the concept of “smart” insulation implemented for the natural convection flow developing inside a differentially heated cavity of 8:1 vertical to horizontal aspect ratio. The rest of the study focuses on generalizing and validating the established concept of “smart” thermo-insulating materials by utilizing square and cubic thermally insulated differentially heated cavities as testbeds. Comprehensive generalization and validation of the established concept will promote the design of “smart” thermo-insulating materials from available off-the-shelf porous materials, which is of significant practical importance.

In section 2.2 the theoretical background regarding 2D and 3D simulations of incompressible natural convection flow in differentially heated cavities is presented. An emphasis is put on the presentation of the physical model and on detailed explanation of the immersed boundary (IB) method (IBM). utilized in the present study to resolve the natural convection flow near the solid boundaries.

In section 2.3 the numerical methodology, established and verified by Gulbeg and Feldman [34], is presented. The idea underlying “smart” thermal insulation is based on the local suppression of the momentum of the natural convection flow. In practice, the implementation of local suppression is based on well-defined criteria. The criteria are formally provided by 2D linear stability analysis augmented by IB functionality. The milestones of the utilized linear stability analysis are given and the validation of the developed methodology for realistic 3D flows is established by utilizing the IB method based on the direct forcing approach.

2.2 3D incompressible natural convection flow

2.2.1 Physical model

The natural convection flow inside a differentially heated cavity is described by the momentum, energy, and continuity equations. These equations are formulated in Cartesian coordinates (x,y,z) with the origin located at one bottom corner of the cavity and gravity (\mathbf{g}) acting opposite to the positive direction of the y axis (see Fig. 2.1).

$$\nabla \cdot \mathbf{u} = 0 \quad (2.1)$$

$$\rho \left(\frac{\partial \mathbf{u}}{\partial t} + (\mathbf{u} \cdot \nabla) \mathbf{u} \right) = -\nabla p + \mu \nabla^2 \mathbf{u} + \rho \mathbf{g} \quad (2.2)$$

$$\frac{\partial T}{\partial t} + (\mathbf{u} \cdot \nabla) T = \alpha \nabla^2 T \quad (2.3)$$

where $\mathbf{u}(u,v,w)$, p , t , and T are the velocity, pressure, time and temperature, respectively, ρ is the fluid's density, μ is the dynamic viscosity and α is the thermal diffusivity. Incompressible flow is assumed. The buoyancy effects are modelled by the Boussinesq approximation - $\rho = \rho_0(1 - \beta(T - T_C))$; this assumption is accurate whenever the density changes can be neglected and when they have no effect on the velocity field except for the ensuing appearance of buoyancy forces. Following [36] and [37], the dimensionless form is utilized using characteristic parameters $L, U = \sqrt{g\beta L\Delta T}$, $t = L/U$ and $P = \rho U^2$ for length, velocity, time, and pressure, respectively. Here, L is the length of the square differentially heated cavity, ρ is the mass density of the working fluid, ρ_0 is the constant density, β is the adiabatic coefficient of thermal expansion, g is gravitational acceleration and $\Delta T = T_H - T_C$ is the temperature difference between the hottest and coldest boundaries. The non-dimensional temperature θ is defined as $\theta = (T - T_C)/\Delta T$. The Ra and Pr numbers are $Ra = \frac{g\beta}{\nu\alpha} \Delta T L^3$ and $Pr = \nu/\alpha$, respectively, where α is the thermal diffusivity and ν is the kinematic viscosity. Consequently, an additional term appears as a source in the y -direction of the Navier-Stokes (NS) equation (Eq. (2.2)), thereby accounting for the temperature-velocity

coupling. The hot and cold walls are held at constant temperatures T_H and T_C , respectively, and all other boundaries are non-slip and perfectly conducting.

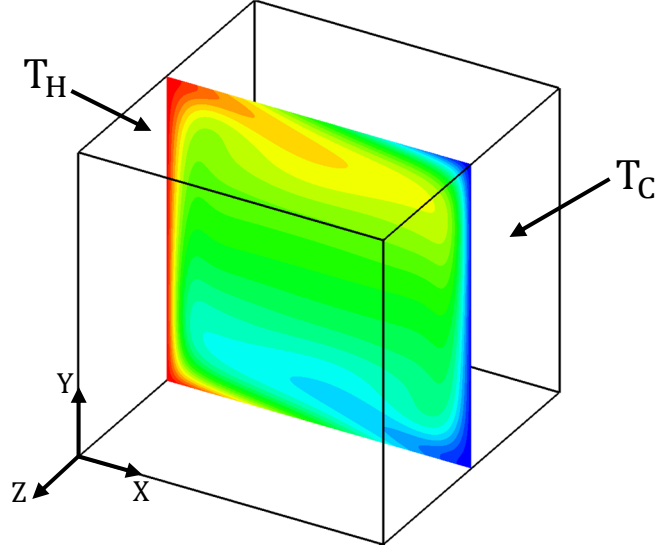


Figure 2.1: Physical model and system of coordinates for the differentially heated cavity. Colors correspond to the temperature distribution at the mid cross section typical of steady state flow.

For the sake of simplicity, the notation of non-dimensional parameters is the same as that used for dimensional ones so that the non-dimensional forms¹ of the continuity equation (Eq. (2.1)), the NS equation (Eq. (2.2)) and the energy equation (Eq. (2.3)) read:

$$\nabla \cdot \mathbf{u} = 0 \quad (2.4)$$

$$\frac{\partial \mathbf{u}}{\partial t} + (\mathbf{u} \cdot \nabla) \mathbf{u} = -\nabla p + \sqrt{\frac{Pr}{Ra}} \nabla^2 \mathbf{u} + \theta \vec{e}_y \quad (2.5)$$

$$\frac{\partial \theta}{\partial t} + (\mathbf{u} \cdot \nabla) \theta = \frac{1}{\sqrt{PrRa}} \nabla^2 \theta \quad (2.6)$$

where $\mathbf{u}(u, v, w)$, p , t , and θ are non-dimensional velocity, pressure, time and temperature variables, respectively, and \vec{e}_y is a unit vector in the vertical (y) direction.

2.2.2 Space and time discretization

¹ Full derivation appears in Appendix C.

The time derivatives in the unsteady momentum and in the energy equations are approximated by using the first order forward Euler's scheme:

$$\frac{\partial s^{n+1}}{\partial t} = \frac{s^{n+1} - s^n}{\Delta t} \quad (2.7)$$

Utilizing the Euler's scheme, Eqs. (2.4), (2.5) and (2.6) can be rewritten as follows:

$$\nabla \cdot \mathbf{u}^{n+1} = 0 \quad (2.8)$$

$$\frac{\mathbf{u}^{n+1} - \mathbf{u}^n}{\Delta t} + (\mathbf{u}^n \cdot \nabla) \mathbf{u}^n = -\nabla p + \sqrt{\frac{Pr}{Ra}} \nabla^2 \mathbf{u}^{n+1} + \theta^{n+1} \vec{e}_y \quad (2.9)$$

$$\frac{\theta^{n+1} - \theta^n}{\Delta t} + (\mathbf{u}^n \cdot \nabla) \theta^n = \frac{1}{\sqrt{PrRa}} \nabla^2 \theta^{n+1} \quad (2.10)$$

After carrying out the time discretization, Eqs. (2.8), (2.9) and (2.10) are presented in a block matrix form:

$$\begin{bmatrix} H_u & 0 & 0 & 0 & -\nabla_p^x \\ 0 & H_v & 0 & \vec{e}_y & -\nabla_p^y \\ 0 & 0 & H_w & 0 & -\nabla_p^z \\ 0 & 0 & 0 & H_\theta & 0 \\ \nabla_u^x & \nabla_v^y & \nabla_w^z & 0 & 0 \end{bmatrix} \begin{bmatrix} u \\ v \\ w \\ \theta \\ p \end{bmatrix} = \begin{bmatrix} RHS_u \\ RHS_v \\ RHS_w \\ RHS_\theta \\ 0 \end{bmatrix} \quad (2.11)$$

Here, $H_u = H_v = H_w = \sqrt{\frac{Pr}{Ra}} \Delta - I/\Delta t$ and $H_\theta = \frac{1}{\sqrt{PrRa}} \Delta - I/\Delta t$ are the Helmholtz operators for the scalar momentum and the energy equations, respectively, I is the identity operator, Δ is the Laplacian operator and $\nabla^x, \nabla^y, \nabla^z$ are the first derivatives with respect to the x, y and z coordinates, respectively. The discrete differential operators on the LHS of Eq. (2.11) can contain different boundary conditions and, therefore, for the general case, $H_u \neq H_v \neq H_w$ and $\nabla_u^x \neq \nabla_v^x, \nabla_v^y \neq \nabla_p^y, \nabla_w^z \neq \nabla_p^z$. Dealing with the spatial differentiation² the LHS of Eq. (2.11), known as the Stokes operator, is further discretized with a standard staggered mesh second-order conservative finite-volume formulation

² Full spatial differentiation can be seen in [55].

[36], while the non-linear terms, moved to the RHS of Eq. (2.11), are approximated by the conservative central differencing scheme to avoid the appearance of artificial numerical viscosity in the upwind scheme (see Ref. [37] for the discretization details).

2.3 “Smart” thermal insulation – concept

The concept of “smart” thermo-insulation is an engineering representation in which the thermal insulator is built of heterogeneous porous material intelligently placed in the bulk of confined natural convection flow to significantly decrease the convective component of heat flux. The porous medium is modelled by unconnected packed beds consisting of immersed bodies – equi- or non-equi-sized cylinders. In this section, the criterion for intelligent placement of the immersed bodies and the method for resolving the flow in the vicinity of the immersed bodies are described. The concept of “smart” thermo-insulating is formally established by utilizing the linear stability analysis of 2D natural convection flows augmented by the IB functionality. The obtained 2D results are further validated by performing the numerical solution of full 3D NS and energy equations for realistic 3D configurations.

The implemented numerical methodology, utilized for solving the 2D modelled flow, is based on the implicit formulation of the IB method and a fully pressure-velocity coupled approach. The methodology incorporates two solvers: a steady state solver based on the full Newton iteration and a linear stability solver for calculating the necessary part of the whole spectrum of the flow by utilizing the Arnoldi iteration method. The two solvers are based on a previously developed [38] fully pressure-velocity coupled direct (FPCD) solver, briefly described in section 2.3.2 for the sake of completeness.

The methodology utilized for solving the 3D NS and energy equations is based on implementation of the segregated (SIMPLE) method augmented by the IB functionality based on the direct forcing approach, as described in section (2.3.5).

2.3.1 Immersed boundary (IB) method

The IBM [39] was developed to resolve the flow near the complex boundaries of immersed bodies when the body surface is either moving or stationary. The key advantage of IBMs is that simulations can still be performed on Cartesian structured grids, thereby facilitating efficient exploitation of the simple structure of the algebraic stencils that are used for spatial discretization of the NS and energy equations. The impact of the body immersed into the flow on the surrounding fluid is expressed in terms of volumetric forces comprising kinematic constraints to enforce non-slip boundary conditions on the body surfaces. These forces appear as additional unknown variables, whose values – along with those for the pressure, temperature and velocity fields – are provided by solving the NS equation and are directly accounted for in the overall balance. The IBM is not a stand-alone solver; rather, it is typically embedded into an existing “driver” (numerical solver initially developed without IB functionality) and should be perceived as a “philosophy” of enforcing boundary conditions. In this study, the IBM was implemented for imposing non-slip boundary conditions at the surfaces of the unconnected packed beds immersed in the convective flow. It should be noted that in the present implementation the immersed bodies must neither intersect nor touch each other, and the minimal distance between the two adjacent IBs is at least the size of a single grid cell. The detailed IBM formulation implemented in the present study is described in the following. Fig. 2.2 shows the setup of a typical spatial discretization implemented on a staggered grid, characterized by an offset between the velocity field and the fields of temperature and pressure. The Eulerian grid points are defined as $\mathbf{x}_i = (x_i, y_i)$. An arbitrary immersed object, B , within a computational domain, D_o , (whose geometry does not, in general, have to conform to the underlying spatial grid) is represented by the surface, ∂B , determined by a set of Lagrangian points, \mathbf{X}_k . The same distance between neighboring points, approximately equal to the grid size, should be preserved to provide high accuracy [40].

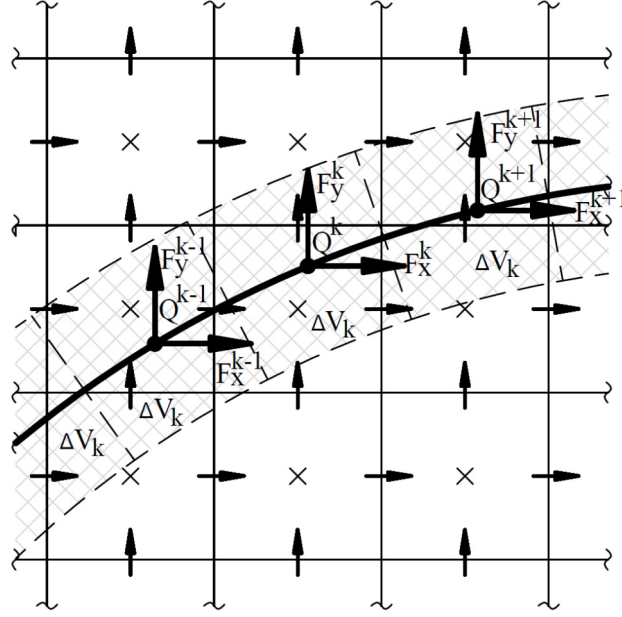


Figure 2.2: A schematic staggered grid discretization of a 2D computational domain D_o , with a slice of IB formulation for a body, B . The virtual shell, whose thickness is equal to the grid cell width, is shaded to distinguish it from the rest of the grid. The horizontal and vertical arrows (\rightarrow, \uparrow) represent the discrete velocity locations, u_i and v_i , respectively. The pressure p_j and the temperature T_j are applied at the center of each grid cell and designated by (\times). Lagrangian points $\mathbf{X}_k = (\xi_k, \psi_k)$ along ∂B are shown as black dots (\cdot) where volumetric boundary forces $\mathbf{F}_k = (\mathbf{F}_{kx}, \mathbf{F}_{ky})$ and volumetric boundary heat fluxes, Q_k , are applied [33].

We next associate a discrete volume dV_k with each Lagrangian point \mathbf{X}_k such that an ensemble of these volumes forms a thin shell with a thickness equal to the width of the grid cell. At the Lagrangian points, appropriate surface forces, \mathbf{F}_k , and heat fluxes, Q_k , are applied to enforce the non-slip velocity and the Dirichlet temperature boundary conditions along ∂B . Since the location of the Lagrangian boundary points does not necessarily coincide with the underlying spatial discretization, regularization and interpolation operators must be defined to convey information about the immersed body in both directions. The regularization operator, \mathbf{R} , smears volumetric forces, \mathbf{F}_k , and heat fluxes, Q_k , on the nearby computational domain, while the interpolation operator, \mathbf{I} , acts in the opposite direction and imposes non-slip/thermal boundary conditions on the points located on the body surface:

$$\mathbf{R}(\mathbf{F}_k(\mathbf{X}_k), Q_k(\mathbf{X}_k)) \equiv \int_S (\mathbf{F}_k(\mathbf{X}_k), Q_k(\mathbf{X}_k)) \cdot \delta(\mathbf{x}_i - \mathbf{X}_k) dV_{Sk} \quad (2.12)$$

$$I(\mathbf{u}(\mathbf{x}_i), \theta(\mathbf{x}_i)) \equiv \int_{\Omega} (\mathbf{u}(\mathbf{x}_i), \theta(\mathbf{x}_i)) \cdot \delta(\mathbf{x}_i - \mathbf{X}_k) dV_{\Omega i} \quad (2.13)$$

where \mathcal{S} corresponds to all cells belonging to the immersed body surface, Ω corresponds to a group of flow cells located in the close vicinity of the immersed body surface, dV_{Sk} corresponds to the infinitesimal volume surrounding each Lagrangian point, \mathbf{k} , and $dV_{\Omega i}$ is the volume of the corresponding flow cell, whose velocity and temperature values are explicitly involved in enforcing boundary conditions at point \mathbf{k} of the immersed body. Convolutions with the Dirac delta function are used to facilitate the exchange of information to and from $\partial\mathcal{B}$. Among the variety of discrete delta functions available, the function described by Roma et al. [41], which is specifically designed for use on staggered grids where even/odd de-coupling does not occur, was chosen. This delta function was successfully utilized in a number of previous studies, [42], [40], [41], [43].

$$\delta(r) = \begin{cases} \frac{1}{6\Delta r} \left[5 - 3\frac{|r|}{\Delta r} - \sqrt{-3\left(1 - \frac{|r|}{\Delta r}\right)^2 + 1} \right] & 0.5\Delta r \leq |r| \leq 1.5\Delta r \\ \frac{1}{3\Delta r} \left[1 + \sqrt{-3\left(\frac{|r|}{\Delta r}\right)^2 + 1} \right] & |r| \leq \Delta r \\ 0 & \textit{otherwise} \end{cases} \quad (2.14)$$

Δr is the cell width in the r direction. The discrete delta function $\delta(r)$ is supported over only three cells, which comprises an advantage for computational efficiency.

The discrete form of regularization and interpolation operators for the 3D domain are governed by:

$$(\mathbf{f}_i, q_i) = \Delta x^3 \sum_k (\mathbf{F}_k, Q_k) \cdot \delta(\xi_k - x_i) \cdot \delta(\psi_k - y_i) \cdot \delta(\zeta_k - z_i) \quad (2.15)$$

$$(\mathbf{U}_k, \Theta_k) = \Delta x^3 \sum_k (\mathbf{u}_i, \theta_i) \cdot \delta(x_i - \xi_k) \cdot \delta(y_i - \psi_k) \cdot \delta(z_i - \zeta_k) \quad (2.16)$$

\mathbf{f}_i and q_i are the discrete volumetric force and heat source defined on the staggered grid (x_i, y_i, z_i) and \mathbf{U}_k, θ_k are the discrete boundary velocity and temperature defined at the $k - th$ Lagrangian point (ξ_k, ψ_k, ζ_k) .

2.3.2 Fully pressure-velocity coupled direct (FPCD).

We consider the 2D formulation of the natural convection flows, in which buoyancy is introduced by the Boussinesq approximation.

The phenomenon is governed by the continuity, NS and energy equations for incompressible flow:

$$\nabla \cdot \mathbf{u} = 0 \quad (2.17)$$

$$\frac{\partial \mathbf{u}}{\partial t} + (\mathbf{u} \cdot \nabla) \mathbf{u} = -\nabla p + \sqrt{\frac{Pr}{Ra}} \nabla^2 \mathbf{u} + \theta \vec{e}_y \quad (2.18)$$

$$\frac{\partial \theta}{\partial t} + (\mathbf{u} \cdot \nabla) \theta = \frac{1}{\sqrt{PrRa}} \nabla^2 \theta \quad (2.19)$$

where $\mathbf{u}(u, v)$, p , Pr , Ra , θ are the non-dimensionalized velocity vector, the pressure field, the Prandtl number, the Rayleigh number and the temperature, respectively, and \vec{e}_y is the unit vector in the opposite direction to gravity. By applying a second-order backward finite difference scheme for the time discretization, Eqs. (2.17)-(2.19) can be rewritten as:

$$\nabla \cdot \mathbf{u}^{n+1} = 0 \quad (2.20)$$

$$\left[\sqrt{\frac{Pr}{Ra}} \nabla^2 \mathbf{u} - \frac{3}{2\Delta t} \mathbf{u} + \theta^{n+1} \vec{e}_y \right]^{n+1} - \nabla p = \left[(\mathbf{u} \cdot \nabla) \mathbf{u} - \frac{2}{\Delta t} \mathbf{u} \right]^n + \frac{1}{2\Delta t} \mathbf{u}^{n-1} \quad (2.21)$$

$$\left[\frac{1}{\sqrt{PrRa}} \nabla^2 \theta - \frac{3}{2\Delta t} \theta \right]^{n+1} = \left[(\mathbf{u} \cdot \nabla) \theta - \frac{2}{\Delta t} \theta \right]^n + \frac{1}{2\Delta t} \theta^{n-1} \quad (2.22)$$

Note that all the non-linear terms are taken from the previous time step and moved to the RHS of the above equations. This system can be compactly written in a block matrix form as:

$$\begin{bmatrix} H_u & 0 & 0 & -\nabla_p^x \\ 0 & H_v & \vec{e}_y & -\nabla_p^y \\ 0 & 0 & H_\theta & 0 \\ \nabla_u^x & \nabla_v^y & 0 & 0 \end{bmatrix} \begin{bmatrix} u^{n+1} \\ v^{n+1} \\ \theta^{n+1} \\ p \end{bmatrix} = \begin{bmatrix} RHS_u^n \\ RHS_v^n \\ RHS_\theta^n \\ 0 \end{bmatrix} \quad (2.23)$$

Here, $H_u = H_v = H_w = \sqrt{\frac{Pr}{Ra}}\Delta - 3I/2\Delta t$ and $H_\theta = \frac{1}{\sqrt{PrRa}}\Delta - 3I/2\Delta t$ are the Helmholtz operators for the scalar momentum and the energy equations, respectively; all of the other terms in the Stokes operator are the same as in section (2.2.2). Following Refs. [37], [38], the fully pressure-velocity coupled solution of Eq. (2.23) can be obtained by *LU*-factorization of the Stokes operator with a set of suitable boundary conditions for all the velocity components and a single Dirichlet reference point for the pressure field. The discrete Stokes operator remains unchanged during the solution, reducing the time integration of the NS equations to two backward substitutions at each time step. The high efficiency of the above approach (see Ref. [37] for the characteristic computational times) is achieved by utilizing a modern multifrontal direct solver for sparse matrices (MUMPS), exploiting the sparseness of the discrete Stokes operator at both *LU* factorization and back substitution stages.

Immersed boundary augmentation

Note that the discrete pressure p appearing in Eq. (2.23) does not actively participate in time propagation and, therefore, can be viewed as the Lagrange multiplier that constrains the solenoidal velocity field. It is therefore reasonable to augment the

existing Stokes operator with IB functionality by adding an additional set of Lagrange multipliers to enforce the appropriate boundary conditions at the Lagrangian points. The equations representing the following augmented Stokes operator are:

$$\nabla \cdot \mathbf{u} = 0 \quad (2.24)$$

$$\frac{\partial \mathbf{u}}{\partial t} + (\mathbf{u} \cdot \nabla) \mathbf{u} = -\nabla p + \sqrt{\frac{Pr}{Ra}} \nabla^2 \mathbf{u} + \theta \vec{e}_y + \mathbf{R}_F \quad (2.25)$$

$$\frac{\partial \theta}{\partial t} + (\mathbf{u} \cdot \nabla) \theta = \frac{1}{\sqrt{PrRa}} \nabla^2 \theta + \mathbf{R}_Q \quad (2.26)$$

$$\mathbf{I}(\mathbf{u}) = \mathbf{U}_b \quad (2.27)$$

$$\mathbf{I}(\theta) = \Theta_b \quad (2.28)$$

Formally, the 2D formulation of the motion equation in its compact matrix form, with the extension of IB (Eqs. (2.24)-(2.28)), is formulated as:

$$\left[\begin{array}{cccc|ccc} H_u & 0 & 0 & -\nabla_p^x & R_{F_x} & 0 & 0 \\ 0 & H_v & \vec{e}_y & -\nabla_p^y & 0 & R_{F_y} & 0 \\ 0 & 0 & H_\theta & 0 & 0 & 0 & R_Q \\ \nabla_u^x & \nabla_v^y & 0 & 0 & 0 & 0 & 0 \\ \hline I_u & 0 & 0 & 0 & 0 & 0 & 0 \\ 0 & I_v & 0 & 0 & 0 & 0 & 0 \\ 0 & 0 & I_\theta & 0 & 0 & 0 & 0 \end{array} \right] \begin{bmatrix} \mathbf{u}^{n+1} \\ \mathbf{v}^{n+1} \\ \theta^{n+1} \\ p \\ F_x \\ F_y \\ Q \end{bmatrix} = \begin{bmatrix} RHS_u^{n-1,n} \\ RHS_v^{n-1,n} \\ RHS_\theta^{n-1,n} \\ 0 \\ U_b \\ V_b \\ \Theta \end{bmatrix} \quad (2.29)$$

The dashed lines appearing in Eq. (2.29) separate between the “original” Stokes operator, located at the top left corner of the matrix and the additional IB entries appearing in Eqs. (2.27)-(2.28). It also separates the corresponding elements appearing in the vector of unknowns and the RHS vector. These additional entries are formally divided into two types. The first type corresponds to the “weights” of the unknown non-dimensional volumetric forces and heat source, F_x , F_y , and Q , respectively, obtained by applying the regularization operator R smearing the forces and heat source over the vicinity of the Lagrangian points (R_{F_x}, R_{F_y}, R_Q). The second type corresponds to the “weights” of the

unknown non-dimensional Eulerian velocity and temperature components I_u, I_v and I_θ , respectively, imposing Dirichlet boundary conditions at the neighboring Lagrangian points. To precisely impose non-slip boundary conditions, the sum of the “second type weights”, each multiplied by its Eulerian velocity component, should be equal to the velocities of the corresponding Lagrangian points U_b and V_b – which represent the velocity of the immersed object. In other words, entries of the second type are nothing more than the additional equations necessary to achieve closure of the whole system of Eq. (2.29), after the unknown forces and heat source, F_x, F_y , and Q , have been added. It should be noted that as a result of the utilization of the same Dirac delta functions, Eq. (2.14), in both the interpolation and regularization operators (\mathbf{I} and \mathbf{R}) and the same uniform staggered grid in the near vicinity of the immersed body surface, the interpolation and regularization operators are transposed to each other, $R_F = I_u^T$. Note also that for all rigid stationary immersed bodies the values of U_b and V_b are all equal to zero, and for time propagation solvers the extended Stokes operator in Eq. (2.29) does not vary in each time step. In this study, the FPCD solver is used to solve a 2D steady state flow, as detailed in the following subsections. As a result of the constant Stokes operator, LU factorization of the extended Stokes operator should be performed only once at the beginning of the computational procedure. For a problem involving moving or deforming bodies, the location of the Lagrangian points is updated at each time step, therefore requiring modification of the extended Stokes operator, as well as its subsequent LU factorization. The factorization of the extended Stokes operator, as well as the “basic” Stokes operator, can be efficiently performed on a massively parallel machine, taking advantage of the high scalability parallelization built into the MUMPS solver [44].

Precise estimation of the average \overline{Nu} number comprises an essential criterion for verification of any numerical solver and is particularly critical for the IBM. The IBM relies on a uniform Cartesian grid, which does not allow further local stretching for a

more precise resolution of the thinnest boundary layers. In this case, a more precise estimation of the \overline{Nu} values is achieved by utilizing the law of conservation of heat flux, rather than simply calculating the near-surface temperature gradient.

Implementing the IB method restricts the grid to be uniform where $\Delta x = \Delta y$ - the dimension of the uniform Eulerian grid. The \overline{Nu} value averaged over the vertical boundaries of the cavity reads:

$$\overline{Nu} = \frac{1}{N} \sum_{i=1}^N \frac{\partial \theta}{\partial x} \quad (2.30)$$

where the local $\frac{\partial \theta}{\partial x}$ values at every point of the vertical boundaries (N) are provided by the solution of Eq. (2.29).

2.3.3 Steady state immersed boundary FPCD solver

The steady state equations, solved by the FPCD solver, representing the incompressible buoyancy driven flow are:

$$\nabla \cdot \mathbf{u} = 0 \quad (2.31)$$

$$(\mathbf{u} \cdot \nabla) \mathbf{u} + \nabla p - \sqrt{\frac{Pr}{Ra}} \nabla^2 \mathbf{u} - \theta \overline{\mathbf{e}}_y = 0 \quad (2.32)$$

$$(\mathbf{u} \cdot \nabla) \theta - \frac{1}{\sqrt{PrRa}} \nabla^2 \theta = 0 \quad (2.33)$$

The IBM, incorporated into a pressure-velocity coupled direct solver, is implemented by introducing the previously defined regularization and interpolation operators. The values of boundary force \mathbf{F}^* and volumetric heat flux Q^* in Lagrangian points are implicitly obtained as a part of the overall solution. The steady state natural convection incompressible flow with an embedded IB functionality is governed by the following equations:

$$\nabla \cdot \mathbf{u} = 0 \quad (2.34)$$

$$(\mathbf{u} \cdot \nabla) \mathbf{u} + \nabla p - \sqrt{\frac{Pr}{Ra}} \nabla^2 \mathbf{u} - \theta \vec{e}_y - R_F = 0 \quad (2.35)$$

$$(\mathbf{u} \cdot \nabla) \theta - \frac{1}{\sqrt{PrRa}} \nabla^2 \theta - R_Q = 0 \quad (2.36)$$

$$I(\mathbf{u}) - U_b = 0 \quad (2.37)$$

$$I(\theta) - \Theta_b = 0 \quad (2.38)$$

Boussinesq approximation is utilized for simulating the buoyancy effects. Additional entries, R_F , R_Q , $I(\mathbf{u})$, $I(\theta)$, are introduced by applying regularization \mathbf{R} and interpolation \mathbf{I} operators to address the impact of the IB on the velocity and temperature fields, by utilizing discrete Dirac delta functions (see Eq. (2.14)). A second order backward finite difference scheme and a standard staggered grid second order conservative finite-volume method are utilized for the temporal and spatial discretization, respectively.

Equations (2.34)-(2.38) can be presented in block matrix form:

$$\begin{bmatrix} J_x & 0 & 0 & J_p & R_{F_x} & 0 & 0 \\ 0 & J_y & \vec{e}_y & J_p & 0 & R_{F_y} & 0 \\ 0 & 0 & J_\theta & 0 & 0 & 0 & R_Q \\ J_u & J_v & 0 & 0 & 0 & 0 & 0 \\ \hline I_u & 0 & 0 & 0 & 0 & 0 & 0 \\ 0 & I_v & 0 & 0 & 0 & 0 & 0 \\ 0 & 0 & I_\theta & 0 & 0 & 0 & 0 \end{bmatrix} \begin{bmatrix} \delta(u) \\ \delta(v) \\ \delta(\theta) \\ \delta(p) \\ \delta(F_x) \\ \delta(F_y) \\ \delta(Q) \end{bmatrix} = - \begin{bmatrix} F_{n_x} - \sum_j R_{jF_x} \\ F_{n_y} - \sum_j R_{jF_y} \\ F_{n_\theta} - \sum_j R_{jQ} \\ F_{n_p} \\ \sum_i I_{iu_x} - U_{b_x} \\ \sum_i I_{iv_y} - V_{b_y} \\ \sum_i I_{i\theta} - \Theta_b \end{bmatrix} \quad (2.39)$$

where J_x , J_y , J_u , J_θ , J_v , J_p are parts of the Jacobian \mathbf{J} of a system of momentum and continuity equations that does not include IB functionality, corresponding to the discrete RHS F_{n_x} , F_{n_y} , F_{n_θ} , F_{n_p} calculated at iteration n . The matrix is expanded by entries of R_{F_x} , R_{F_y} , R_θ and I_u , I_v , I_θ as a result of embedded IB formulation. The IB entries also contribute to the RHS of Eq. (2.39). The volumetric forces F_j and interpolated velocities u_i , both calculated at iteration n , are added to the corresponding RHS of the momentum

and interpolation equations. The index i corresponds to Eulerian points and the index j corresponds to Lagrangian points. The iterative Newton-Raphson method is used to solve Eq. (2.39).

2.3.4 Linear stability immersed boundary FPCD solver

The steady state solution calculated in the previous section was further used for performing a linear stability analysis based on the algorithm previously developed by Gelfgat [45] and extended by the IB functionality. The present method imposes no restriction on the number or shape of the bodies. However, due to the use of the IBM, the bodies should not touch or intersect each other or the boundaries of the cavity and the minimal distance between any neighboring immersed objects or between any immersed object and the cavity boundary shall not be smaller than the size of a single grid cell. We next consider a slightly perturbed steady state solution of the form:

$$\mathbf{u} = \mathbf{U} + \tilde{\mathbf{u}} \quad (2.40)$$

$$\theta = \Theta + \tilde{\theta} \quad (2.41)$$

$$p = P + \tilde{p} \quad (2.42)$$

$$\mathbf{f} = \mathbf{F} + \tilde{\mathbf{F}} \quad (2.43)$$

$$q = Q + \tilde{Q} \quad (2.44)$$

where $\tilde{\mathbf{u}}, \tilde{\theta}, \tilde{p}, \tilde{\mathbf{F}}$ and \tilde{Q} are perturbations of velocity, temperature, pressure and Lagrangian forces fields. Assuming infinitesimally small perturbations in the form of $\{\tilde{\mathbf{u}}(x, y), \tilde{\theta}(x, y), \tilde{p}(x, y), \tilde{\mathbf{F}}(x, y), \tilde{Q}(x, y)\}e^{\lambda t}$ from the steady state flow $\mathbf{U}, \Theta, p, F, Q$, as follows, and substituting them into Eqs. (2.34)-(2.38) yields:

$$\lambda \tilde{\mathbf{u}} = -(\mathbf{U} \cdot \nabla) \tilde{\mathbf{u}} - (\tilde{\mathbf{u}} \cdot \nabla) \mathbf{U} - \nabla \tilde{p} + Gr^{-0.5} \nabla^2 \tilde{\mathbf{u}} - \tilde{\theta} \vec{e}_y - R_{\tilde{\mathbf{F}}} \quad (2.45)$$

$$\lambda \tilde{\theta} = -(\mathbf{U} \cdot \nabla) \tilde{\theta} - (\tilde{\mathbf{u}} \cdot \nabla) \Theta + Pr^{-1} Gr^{-0.5} \nabla^2 \tilde{\theta} + R_{\tilde{Q}} \quad (2.46)$$

$$\nabla \cdot \tilde{\mathbf{u}} = 0 \quad (2.47)$$

$$I(\tilde{\mathbf{u}}) = 0 \quad (2.48)$$

$$I(\tilde{\theta}) = 0 \quad (2.49)$$

where λ is the complex eigenvalue defined as:

$$\lambda = \text{Re}(\lambda) + \text{Im}(\lambda) \quad (2.50)$$

where $\text{Im}(\lambda)$, is the imaginary part of the complex eigenvalue λ , corresponding to the angular frequency of the perturbation (σ), and $\text{Re}(\lambda)$ is the real part of the complex eigenvalue λ corresponding to the growth rate (ω). In linear stability analysis we are typically interested in finding the critical value of the control parameter (e.g. Ra_{cr}) at which $\text{Real}(\lambda) = 0$ (to a prescribed precision), where λ is the leading eigenvalue. Eqs. (2.45)-(2.49) rewritten in a block matrix form yield:

$$\lambda \mathbf{B} \begin{bmatrix} \tilde{\mathbf{u}} \\ \tilde{\theta} \\ \tilde{p} \\ \tilde{\mathbf{F}} \\ \tilde{Q} \end{bmatrix} = \mathbf{J} \begin{bmatrix} \tilde{\mathbf{u}} \\ \tilde{\theta} \\ \tilde{p} \\ \tilde{\mathbf{F}} \\ \tilde{Q} \end{bmatrix} \quad (2.51)$$

where \mathbf{J} is the Jacobian matrix calculated from the RHS of Eqs. (2.45)-(2.49) and \mathbf{B} is the diagonal matrix whose diagonal elements, corresponding to the values of $\tilde{\mathbf{u}}$, $\tilde{\theta}$, are equal to unity, whereas the diagonal elements corresponding to \tilde{p} , $\tilde{\mathbf{F}}$, \tilde{Q} are equal to zero. By this means matrix \mathbf{B} is singular. Note also that since the discretization is performed on a structured staggered grid in Cartesian coordinates, the discrete forms of Jacobians \mathbf{J} appearing in Eqs. (2.39) and (2.51) are the same.

The generalized eigenproblem in Eq. (2.51) cannot be directly transformed into a standard eigenproblem, since $\det(\mathbf{B}) = 0$; instead it is solved in a shift-invert mode

$$(\mathbf{J} - \sigma \mathbf{B})^{-1} \mathbf{B} \begin{bmatrix} \tilde{\mathbf{u}} \\ \tilde{\theta} \\ \tilde{\mathbf{p}} \\ \tilde{\mathbf{F}} \\ \tilde{\mathbf{Q}} \end{bmatrix} = \mu \begin{bmatrix} \tilde{\mathbf{u}} \\ \tilde{\theta} \\ \tilde{\mathbf{p}} \\ \tilde{\mathbf{F}} \\ \tilde{\mathbf{Q}} \end{bmatrix} ; \quad \mu = \frac{1}{\lambda - \sigma} \quad (2.52)$$

The solution is based on a standard Arnoldi iteration implemented within an open source ARPACK package, providing the dominant eigenvalue (i.e. the eigenvalue with the largest modulus).

The dominant eigenvalue μ can be related to the leading eigenvalue λ (i.e. that of a zero real part) when the approach is applied to a shift-invert problem, where σ is a complex shift (see Eqs. (2.52)). In order to converge the approach, the complex shift σ should be close to the leading eigenvalue of λ , the real part of which is close to zero and whose imaginary part $Im(\lambda)$ corresponds to the critical angular oscillating frequency, σ_{cr} . The latter is either known from benchmark problems or can be estimated by a series of successive direct numerical simulations of the slightly bifurcated flow.

The linear stability analysis of a given steady state is studied by applying the shift-inverse Arnoldi iteration to the corresponding eigenvalue problem with the secant method, providing a precise value for the critical control parameter. The overall process requires numerous solutions of large systems of linear equations, which should be performed at each step of the Newton method and while building the Krylov basis for the Arnoldi iteration. Typically, no more than ten iterations are required for the calculation of the steady state solution (by the Newton method), while the shift-invert Arnoldi iteration needs $O(10^4)$ iterations to converge, thus comprising the key issue determining the computational efficiency of the whole process.

The fact that the operator $(\mathbf{J} - \sigma \mathbf{B})^{-1} \mathbf{B}$ does not change during the building of the Krylov basis for the Arnoldi iteration helps the efficiency of the calculation of the

operator $(\mathbf{J} - \sigma\mathbf{B})^{-1}\mathbf{B}$ by the vector $[\tilde{\mathbf{u}} \ \tilde{\theta} \ \tilde{p} \ \tilde{\mathbf{F}} \ \tilde{Q}]^T$ required at each Arnoldi iteration step. The product implementation is simply a solution \mathbf{X} of the linear system $(\mathbf{J} - \sigma\mathbf{B})\mathbf{X} = \mathbf{B}[\tilde{\mathbf{u}} \ \tilde{\theta} \ \tilde{p} \ \tilde{\mathbf{F}} \ \tilde{Q}]^T$. By utilizing the direct solver MUMPS, the \mathbf{LU} decomposition of the operator $(\mathbf{J} - \sigma\mathbf{B})$ is performed once at the beginning of the process, exploiting the sparseness of the matrix, and then each vector of the Krylov basis is obtained by just two subsequent back substitutions – faster than any iterative solver. At the end of this stage, we receive the leading eigenvalue λ , and the leading eigenvectors of all the flow fields are calculated.

2.3.5 Direct forcing approach

Despite being extremely efficient for analysis of 2D flows, the methodology based on a fully coupled pressure-velocity approach is not suitable for realistic 3D problems. This is because both operators described in Eq. (2.39) and in Eq. (2.52) are of the saddle point type, and for realistic 3D problems one should adopt iterative methods employing fractional-step or projection approaches. For a more detailed discussion on this topic, the section *Pros and Cons of the Developed Method* in the recent study of Feldman and Gulberg [34] should be consulted. Therefore, a different – direct forcing – method, incorporated with a segregated approach for the pressure-velocity coupling, is utilized to perform the 3D numerical simulations. The direct forcing method allows for a smooth transition between the Eulerian and Lagrangian representations, while the system of governing NS equations is solved using a SIMPLE method implementing a segregated approach. The purpose of the direct forcing scheme is to impose the desired non-slip velocity at the points belonging to the surface of the immersed body. In this study, the direct forcing approach is based on the work of Kempe and Fröhlich [46]. The direct forcing method approximates the boundary force \mathbf{F}^* and the volumetric heat flux Q^* for rigid bodies with an intermediate predicted velocity field \mathbf{u}^* , initially calculated by

ignoring the presence of the immersed body. The forces at Lagrangian points are calculated explicitly:

$$\mathbf{F}^*(\mathbf{X}_k, t^n) = \frac{\mathbf{U}^\Gamma(\mathbf{X}_k, t^n) - \mathbf{U}^*(\mathbf{X}_k, t^n)}{\Delta t} \quad (2.53)$$

where \mathbf{U}^* represents the values of the boundary velocity obtained by interpolation of the nearby predicted velocity field on the immersed body surface, and \mathbf{U}^Γ corresponds to the preset boundary velocity calculated by the rigid body motion of the solid object $\mathbf{U}^\Gamma(\mathbf{X}_k, t^n) = \mathbf{U}_c + \boldsymbol{\omega} \times (\mathbf{X}_k - \mathbf{X}_c)$, where $\mathbf{U}_c, \boldsymbol{\omega}$ are the translational and rotational velocities and \mathbf{X}_c is the center coordinate of the immersed object (in this study the object is stationary and, therefore, the boundary velocity is zero). The calculated \mathbf{F}^* is smeared over the volumes of the computational domain by utilizing the regularization operator, \mathbf{R} . Computed in this way, discrete volumetric forces \mathbf{f}^* contribute as a source to the momentum equation.

$$\frac{\mathbf{u}^* - \mathbf{u}^n}{\Delta t} + (\mathbf{u}^n \cdot \nabla) \mathbf{u}^n - \mathbf{f}^* = -\nabla p + \sqrt{\frac{Pr}{Ra}} \nabla^2 \mathbf{u}^* + \theta^n \vec{e}_y \quad (2.54)$$

Lastly, the algorithm is finalized by the standard projection-correction step, which includes a solution of the Poisson equation, yielding the fields of corrected pressure and a divergence free velocity vector. The boundary temperature values, Θ^Γ , of the surface of the immersed body are enforced by:

$$\mathbf{Q}^*(\mathbf{X}_k, t^n) = \frac{\Theta^\Gamma(\mathbf{X}_k, t^n) - \Theta^*(\mathbf{X}_k, t^n)}{\Delta t} \quad (2.55)$$

where the temperature at the Lagrangian points Θ^* is an interpolation of the intermediate temperature field θ^* , initially computed by ignoring the presence of the immersed body, and \mathbf{Q}^* is a non-dimensional volumetric heat source, subsequently smeared over adjacent volumes by a regularization operator (Eq. (2.15)). As a result, the regularized volumetric Eulerian heat source, \mathbf{q}^* , enters as a source into the corresponding energy equations:

$$\frac{\theta^* - \theta^n}{\Delta t} + (\mathbf{u}^n \cdot \nabla) \theta^n - q^* = \frac{1}{\sqrt{PrRa}} \nabla^2 \theta^{n+1} \quad (2.56)$$

It should be emphasized that the source/sink q^* value is relevant only if the preset Dirichlet or Neumann boundary conditions have to be enforced (i.e. in the presence of a thermally active immersed surface). If the immersed body is exposed only to convective flow and does not actively emit/absorb the heat by itself, then only non-slip boundary conditions are enforced on the immersed surface. In this case, a zero value is assigned to the q^* term appearing in Eq. (2.56). Formally, this imposes zero thermal resistance in the direction normal to the body surface, in accordance with the assumption of zero wall thickness of embedded obstacles. Note also that, due to the stationary boundaries, the interpolation/regularization operators can be pre-computed for each prescribed immersed surface; there is no need to employ a delta function at each time step, since it will yield the same result, thereby considerably decreasing the computational effort.

Chapter 3: Results and Discussion

3.1 Chapter overview

In this chapter, the results obtained in the framework of the current study are presented and discussed. The first part of the study (section 3.2) focuses on the design of a “smart” thermo-insulator in a differentially heated cavity with an aspect ratio 8:1. The effects of the modelled porous media implants embedded into the bulk of the natural convection flow are discussed in terms of their efficiency in suppressing the momentum of the flow. The impact of optimization parameter \mathbf{A} (related to the perturbation of the kinetic energy of the flow) on the insulation capacity of the modelled porous media implants is discussed.

The second part of the study focuses on statistical evaluation of the number of generated sets of modelled patterns of porous media. The confined natural convection flow inside a differentially heated cubic cavity was chosen as a testbed. A set containing 10 implants of heterogeneous porous media was generated by utilizing both the steady state and the linear stability analysis solvers. Each implant was modelled by unconnected packed beds built of cylinders, whose diameters were drawn in accordance with a Gaussian distribution to encompass the whole set of porous media structures. The procedure of building the whole set of patterns and further statistical evaluation of its insulating properties are discussed in subsection 3.2.2.

The third part of the study is based on the results that were obtained in the previous part and averaged in terms of porosity value, geometric center and shape of the porous media implant. The performed statistical analysis sheds light on the impact of a whole set of porous media structures on the insulating efficiency of the modelled porous media implants. Finally, a 3D validation of the established methodology was performed, revealing trends similar to those observed in 2D flows.

3.2 “Smart” thermal-insulation

The “smart” thermal insulator design method employs a linear stability analysis of natural convection flows in the presence of heterogeneous porous media, as detailed in a recent study of Gulberg and Feldman [35]. Following this work, the presently employed optimization procedure is based on minimizing the value of parameter \mathbf{A} , defined as $\mathbf{A} = |\tilde{u}_x|^2 + |\tilde{u}_y|^2$, where $|\tilde{u}_x|$ and $|\tilde{u}_y|$ are the absolute values of the perturbations of the corresponding velocity components. The optimization procedure is an iterative process which will be described here. The iterations start with the linear stability analysis based on the solution of Eqs. (2.45)-(2.49), performed for the flow within the cavity with no obstacles. As a result, the value of the critical Rayleigh number, Ra_{cr} , for the first Hopf bifurcation is obtained and two cylindrical obstacles are placed at the locations where the criterion \mathbf{A} attains its maximal value³. The corresponding fields of values of \mathbf{A} and of the temperature distribution at steady state, with superimposed streamlines, are shown in Fig. 3.1. In the next step, the linear stability analysis is repeated for the modified flow, which is characterized by a new value of Ra_{cr} , at which a transition to unsteadiness takes place. The next pair of obstacles can again be positioned at places where the new values of \mathbf{A} reach their absolute maximum. In the present study, the above procedure is repeated until a twofold decrease in the average \overline{Nu} number is achieved⁴. Note that the boundary of each cylindrical obstacle is assumed to be of zero thickness; hence there is no need to employ any specific heat fluxes in Eqs. (2.36) and (2.46), nor boundary conditions for the temperature determined by Eqs. (2.38) and (2.49). As a result, the boundaries of the cylinders have no thermal resistance in the direction normal to the body surface.

³ The obstacles always come in pairs due to the skew-symmetry of the flow.

⁴ The procedure can be also applied with another termination criterion.

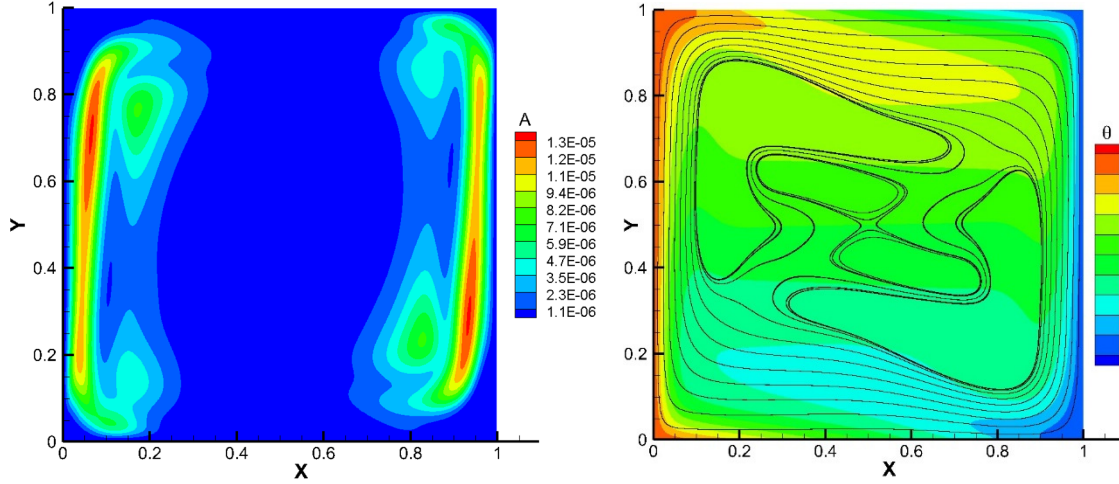


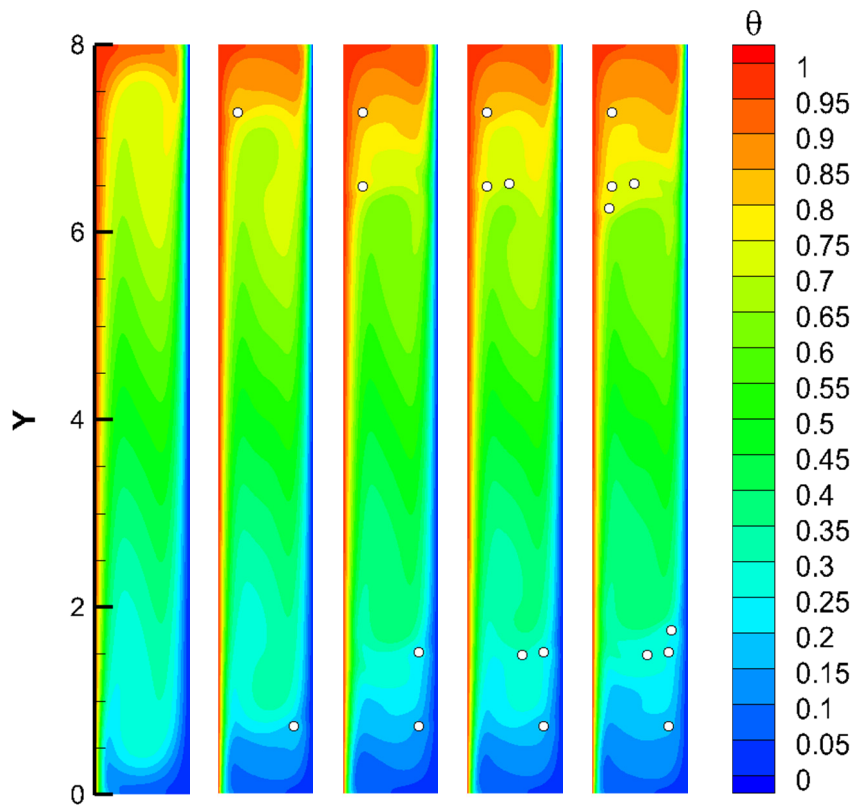
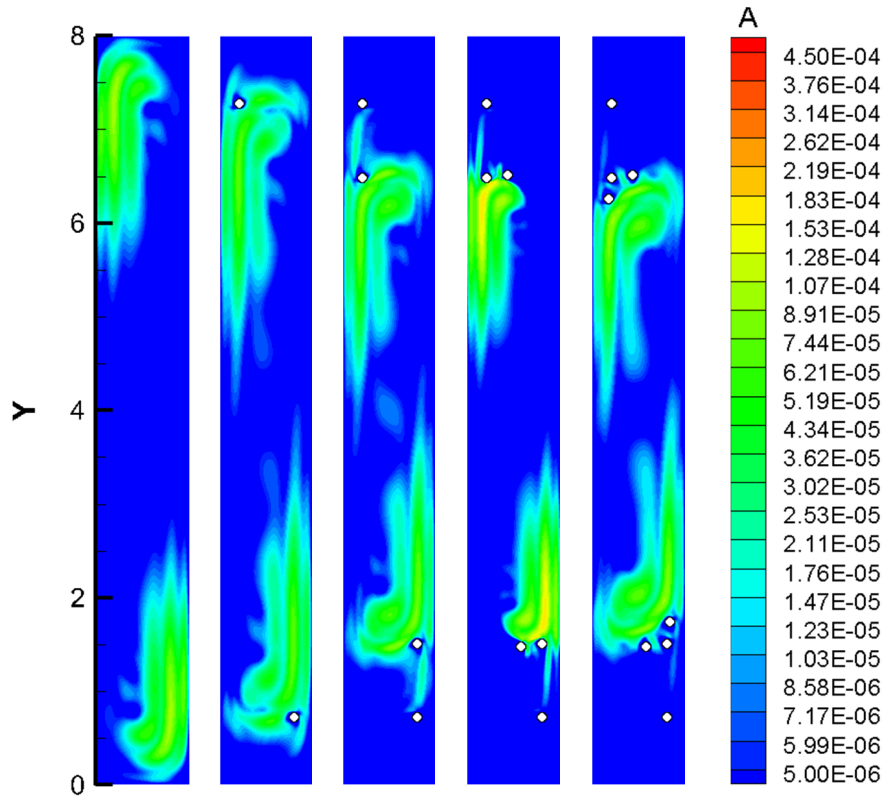
Figure 3.1: Contours of criterion A and the corresponding steady state distribution of temperature, θ , with superimposed streamlines obtained at $Ra = 2.15 \cdot 10^6$ for no obstacles.

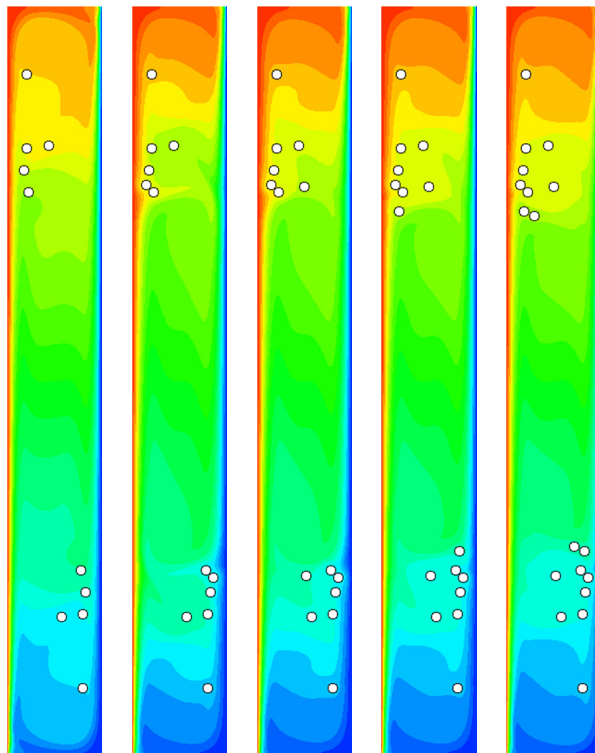
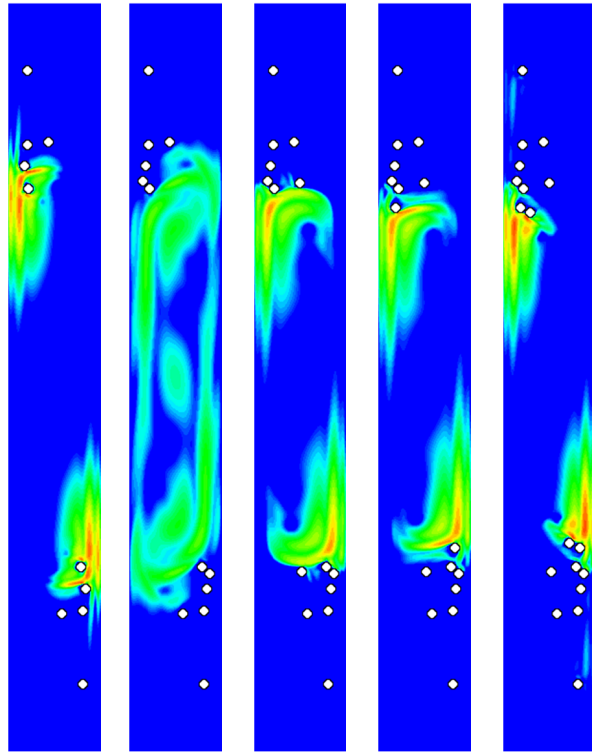
The basic assumption of the optimization methodology implemented in the present study is that the most energetic regions of the 2D convective flow predicted by the linear stability analysis coincide, with an acceptable degree of accuracy, with the corresponding regions observed in the 3D configuration built by extrusion of the corresponding 2D confinement along its normal direction. This idea is supported by the striking similarity existing between the spatial and temporal characteristics observed for 2D and 3D steady and bifurcated flows in differentially heated square and cubic cavities, respectively, with perfectly thermally conducting horizontal boundaries (see e.g. Ref. [47]). The above assumption was successfully validated by the recent study of Gulberg and Feldman [35], who demonstrated about the same enhancement of insulating efficiency of a 2D differentially heated cavity and its 3D counterpart, both optimized by embedded implants of porous media. Following the same principle, the efficiency of all the porous media patterns obtained by the 2D linear stability analysis was validated by the corresponding 3D simulations. The numerical solution of full 3D NS equations (Eqs. (2.24)-(2.28)) was conducted by the recently developed IB solver [48]. Extensive discussion on the implementation and verification of the developed solver for thermal flows in the presence of thermally active and passive immersed bodies can be found in Ref. [48], and is omitted here for the sake of brevity.

3.2.1 2D differentially heated cavity with 8:1 aspect ratio

As a direct continuation of Gulbeg and Feldman's [35] study for the creation of a “smart” thermal insulator methodology, a 2D simulation of a differentially heated cavity was conducted to build a pattern of a porous medium using the steady state and the linear stability analysis solvers for a cavity with an aspect ratio of 8:1. The cavity has perfectly conducting horizontal boundaries, while its vertical left and right boundaries are held at constant hot and cold temperatures, respectively. Utilizing the optimization criterion \mathbf{A} , closely related to the perturbation of kinetic energy, a pattern modelled by unconnected equi-sized cylinders with a diameter of $D = 0.05$ was generated using an iterative process; this process required, first, that at each iteration the cylinder's center is placed at the point with the maximal value of \mathbf{A} and, second, that the minimal distance between the cylinder's boundary and the boundaries of the previously placed cylinders or the cavity walls is at least equal to the size of a single grid step, which is an intrinsic requirement of the discrete Delta functions utilized in the present study [41]. The cylinders (obstacles) are placed in pairs due to the skew-symmetry of the flow. If one of the above criteria is violated, the location of the next largest value of \mathbf{A} is sought and the morphological structure of the current “candidate” of the porous media implant is tested for meeting all the restrictions. Similarly to the previously mentioned study [35], the iterative process of building the pattern is terminated when a twofold decrease in the Nusselt number \overline{Nu} averaged over the cavity vertical boundaries is achieved⁵.

⁵ Heat flux passing through the differentially heated cavity can be estimated by calculating the averaged Nusselt number over the cavity vertical boundaries.





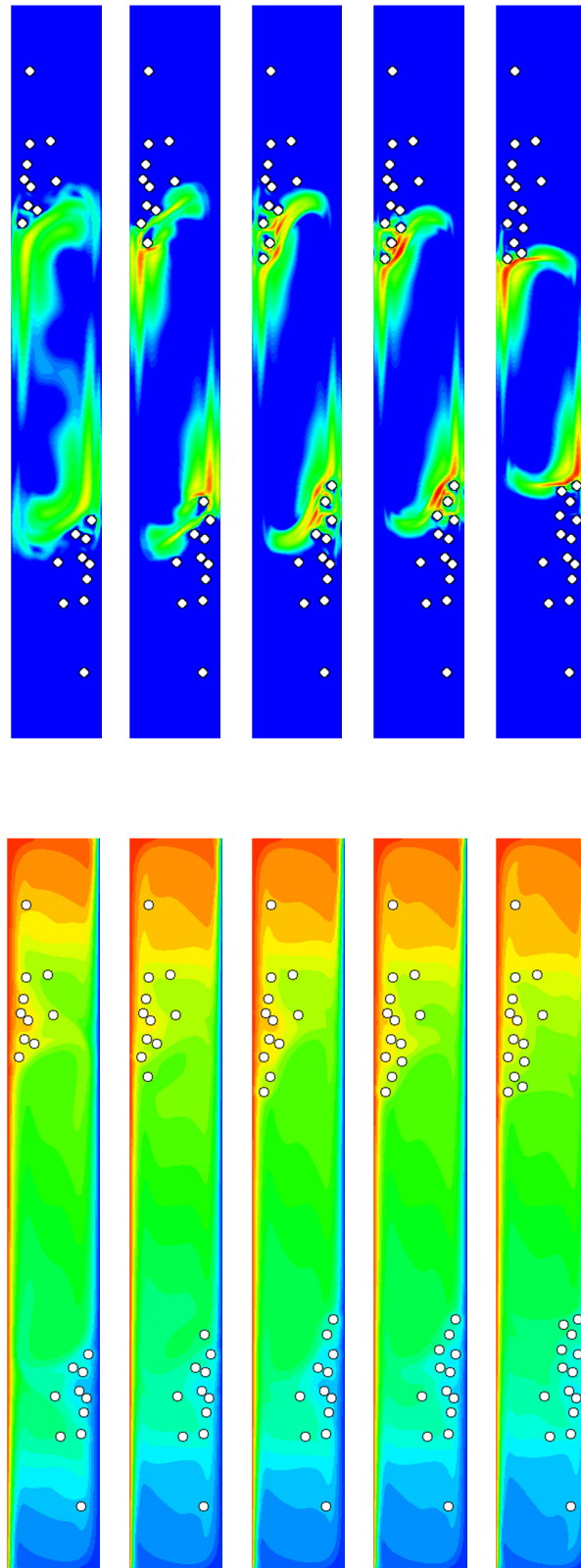


Figure 3.2: Evolutionary stages of the process of generation of implants of “smart” thermal insulator for a differentially heated cavity of aspect ratio 8:1: three pairs of diagrams each show (top) \mathcal{A} criterion. (bottom) the corresponding temperature distribution.

For the non-slip boundary condition, the Nusselt number depends only on the temperature gradient normal to the wall direction. Note that for the steady state flow the temperature distribution is skew-symmetric relative to the cavity center. The stages describing the iterative procedure of implant pattern generation of “smart” porous media are shown in Fig. 3.2. It should be noted that due to the convergence difficulties of the linear stability solver we were able to insert only 28 cylinders into the cavity, and the final goal of a twofold decrease in the value of the averaged Nusselt number, \overline{Nu} , was not achieved. Nevertheless, some representative trends revealed in the course of the generation of the porous media pattern are worth mentioning. First, it is clearly shown that for each pair of inserted cylinders, the active area characterized by non-zero values of the optimization parameter \mathbf{A} converges towards the center of the cavity, which resembles the flow behavior typical of differentially heated square cavities. Consequently, the impact of the cylinders placed in the upper and lower regions (hot and cold boundaries, respectively) of the cavity is less significant than that related to the cylinders placed in the central region of the cavity. The above statement is further confirmed by looking at Fig. 3.3-a, which quantifies the changes in \overline{Nu} as a function of the number of embedded cylinders. Despite the almost monotonic decrease in the value of the average Nusselt number, \overline{Nu} , the decrease rate is not as high as that typical of square differentially heated cavities [35]. Second, as shown in Fig. 3.2, the magnitude of optimization parameter \mathbf{A} increases with the number of embedded cylinders. This observation is apparently a consequence of higher velocity values in the center of the cavity as a result of the blockage effects of embedded cylinders. The process of convergence of the maximal values of optimization parameter \mathbf{A} is followed by a non-monotonic increase in the critical Ra_{cr} value, which starts to exhibit a monotonic rise only after embedding 20 cylinders (see Fig. 3.3-b).

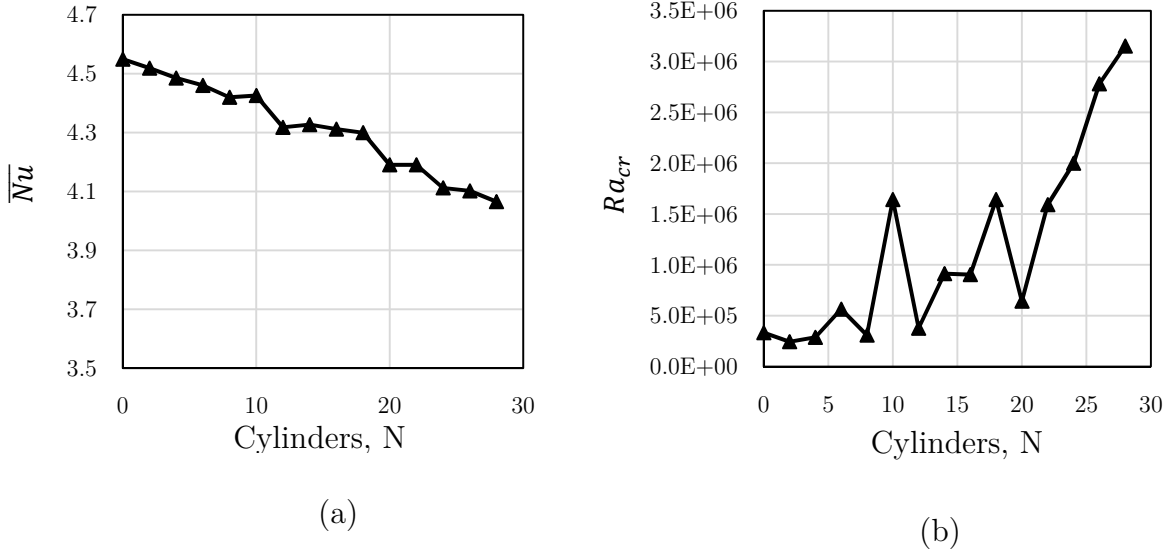


Figure 3.3: (a) Value of the averaged \overline{Nu} number obtained for the vertical hot wall of the cavity at $Ra_{cr} = 3.32 \cdot 10^5$, (b) The critical Rayleigh, Ra_{cr} number for the steady-unsteady transition obtained by the linear stability analysis as a function of the number of cylindrical obstacles for a grid of 800x100.

3.2.2 Generalized “smart” thermo-insulator in a cubical differentially heated cavity

Following the recent work of Gulbeg and Feldman [35], all the 2D calculations that included calculation of the steady state flow and its subsequent linear stability analysis were performed on a 500×500 uniform grid, thus providing grid independence of the obtained results. This study aimed at the generalization of the concept of “smart” thermal insulators in the context of decreasing convective heat flux through air-filled cavities of hollow construction blocks. To check the impact of porosity as a macro-optimization parameter determining the insulating properties of the modelled heterogeneous porous media, we start with the most general configuration and build a set of 10 different patterns, each consisting of non-equi-sized cylinders. The diameters of the cylinders in each pattern were drawn in accordance with a Gaussian distribution characterized by an average value of $D_{av} = 0.1$ and standard deviation of $\sigma = \pm 0.02$. The patterns were built by an iterative process: first, the cylinder center was placed at the point with the maximal value of criterion **A**; second, the minimal distance between the cylinder's boundary and the boundaries of the previously placed cylinders (for the

second and subsequent placements) or the cavity walls was fixed to be at least the size of a single grid step. The second step is an intrinsic requirement of the discrete Delta functions utilized in the present study [41] for the implementation of interpolation I and regularization R operators. If the second condition could not be met, a new diameter of the subsequent cylinder was drawn. An additional limitation to be considered is related to the scenario where the distance between the point characterized by the maximal value of criterion \mathbf{A} and the closest boundary is smaller than the minimal allowed value of the cylinder radius ($D_{av}/2 - 1.5\sigma$). In this case the location of the next largest value of \mathbf{A} is sought and the morphological structure of the new "candidate" of the porous media implant is tested to verify that it complies with all the conditions.

In Figs. 3.4 and 3.5, two typical sequences of the construction of different porous media patterns are shown, corresponding to the porous media materials characterized by the minimal ($\phi = 0.51$) and maximal ($\phi = 0.64$) values of porosity (from the set of 10 different patterns), respectively. Colors represent the corresponding distributions of the control parameter \mathbf{A} . Note that only a single pair of cylinders was added at each iteration (due to the skew-symmetry of the flow) and, therefore, Figs. 3.4 and 3.5 show only a number of representative configurations. The final geometry of both implants⁶, yielding a twofold decrease in the Nusselt number, \overline{Nu} , averaged over the cavity vertical boundaries, is confined by the white curve (see Figs. 3.4-f and 3.5-f). Note that in the present study the porosity of the porous media implant is defined as:

$$\phi = \left(V_p - \sum_{N_{cyl}} V_N \right) / V_p, \quad (3.1)$$

where V_p is the volume of the final configuration of the porous media implant.

⁶ The contours comprise closed Bezier curves of the third order (see Appendix A for more details).

Despite the evident differences between the structures of both patterns, a number of trends, which will be exploited for further generalization of the strategies for the design of “smart” thermally-insulating materials, can be clearly recognized.

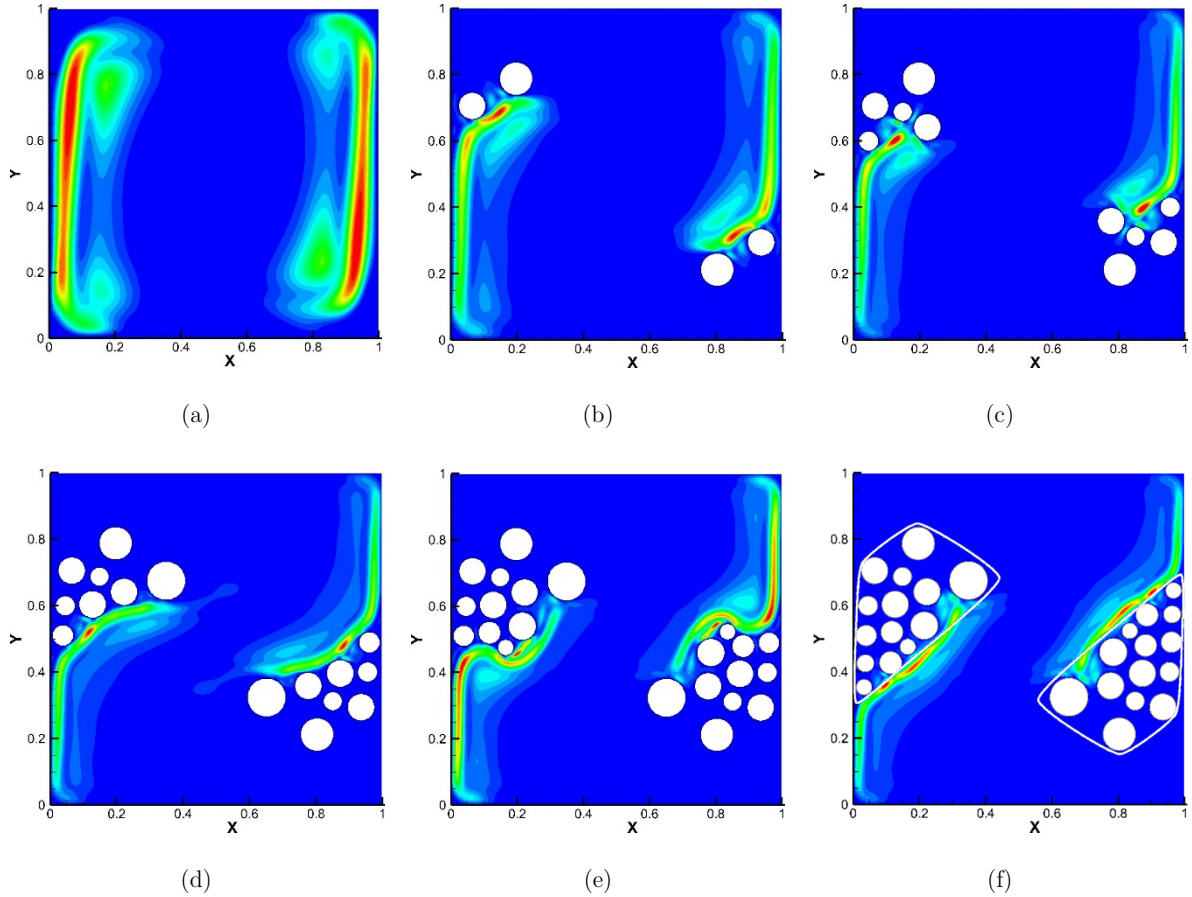


Figure 3.4: Successive stages of building the pattern of “smart” insulators characterized by the minimal porosity value, $\phi = 0.51$. The final pattern of the porous material is confined by the white solid line. The colors correspond to the distribution of the control parameter \mathbf{A} . Figure (f) was obtained at $Ra = 4.39 \times 10^7$.

First, both patterns have the shape of a bunch of grapes close to the hot vertical boundary (or the shape of inverted bunch of grapes close to the cold vertical boundary), and are flattened in the vicinity of the vertical walls. Second, the geometric center of both configurations is much closer to the vertical compared to the horizontal walls of the cavity. Third, the convective flows that initially rise or descend along the vertical hot and cold walls, respectively, are further redirected to the cavity center. As a result, the close vicinity of vertical walls of the cavities with embedded implants of porous medium is characterized by a more uniform distribution of the temperature (see Fig.

3.6). This, in turn, results in lower temperature gradients and, as a consequence, in lower values of the local \overline{Nu} number. It is remarkable that the same trends were also observed for all other configurations from the same set characterized by the intermediate porosity values, as summarized in Table 1. Fig. 3.7 quantifies the dependence of the average \overline{Nu} and the steady-unsteady critical Ra_{cr} values versus the number of embedded cylinders observed for the porous media patterns characterized by the maximal and minimal porosity values. Note that the similar monotonic decrease in \overline{Nu} and intermittent increase in Ra_{cr} values as a function of the number of embedded cylinders was observed in [35] for the porous media patterns modelled by unconnected packed beds of equi-sized cylinders. It is interesting that, although \overline{Nu} monotonically decreases, non-monotonic behavior is observed for Ra_{cr} , which could be related to the non-linearity of the system and reflects different physical branches existing for the same parameters.

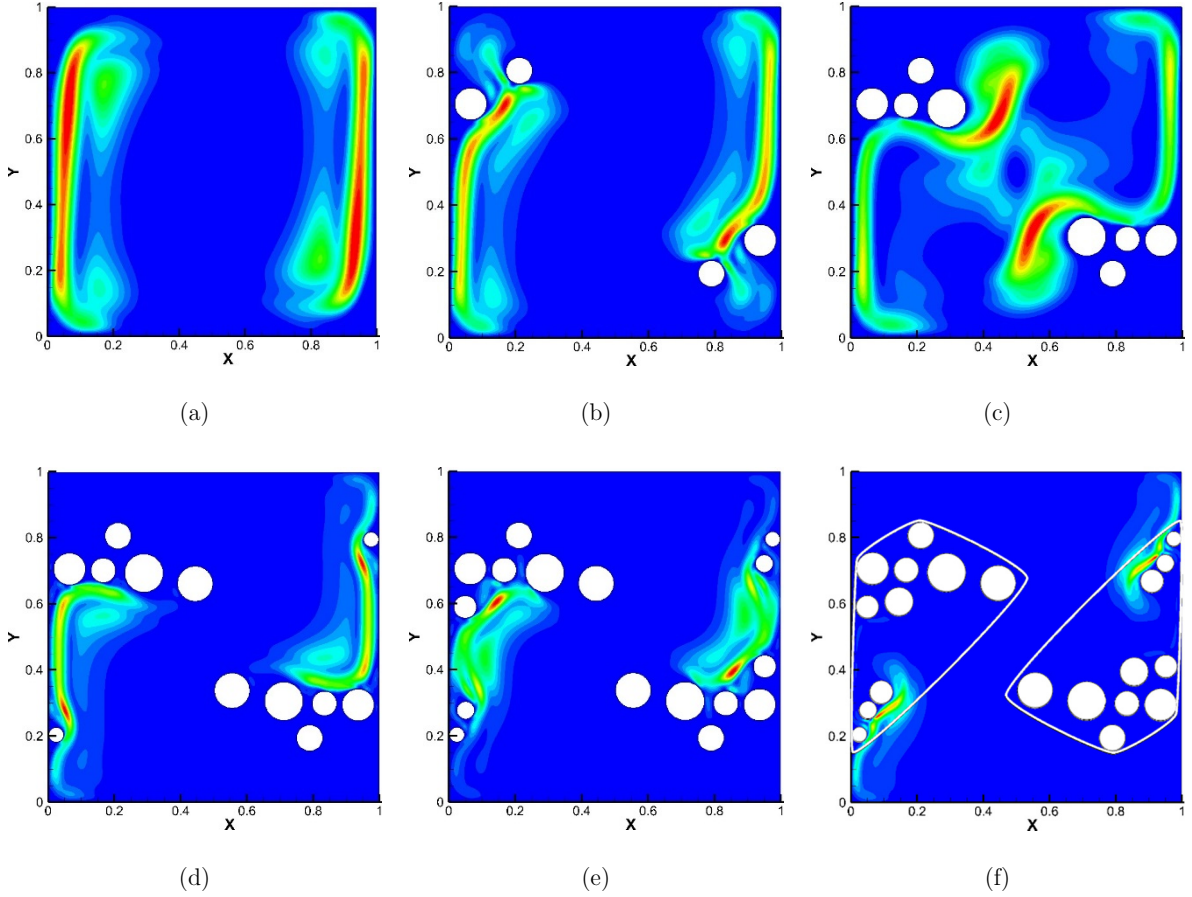


Figure 3.5: Successive stages of building the pattern of “smart” insulators characterized by the maximal porosity value, $\phi = 0.64$. The final pattern of the porous material is confined by the white solid line. The colors correspond to the distribution of the control parameter \mathbf{A} . Figure (f) was obtained at $Ra = 5.13 \times 10^7$.

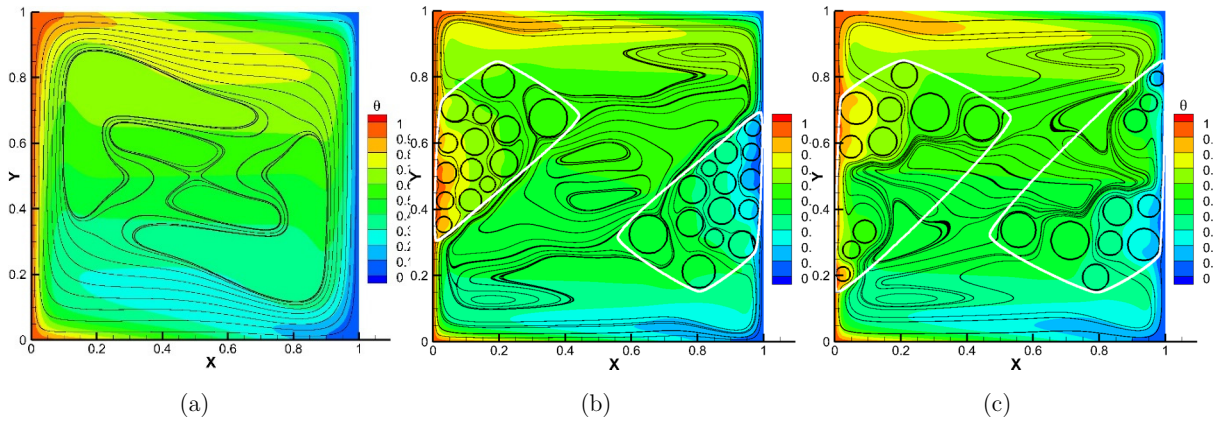


Figure 3.6: Temperature distribution with superimposed streamlines for: (a) Configuration without porous implants obtained for $Ra = 2.15 \times 10^6$, (b) Configuration with porous implants characterized by $\phi = 0.51$ obtained for $Ra = 4.39 \times 10^7$, (c) Configuration with porous implants characterized by $\phi = 0.64$ obtained for $Ra = 5.13 \times 10^7$. The transparency of the cylinders stresses the fact that their boundaries have zero thermal resistance.

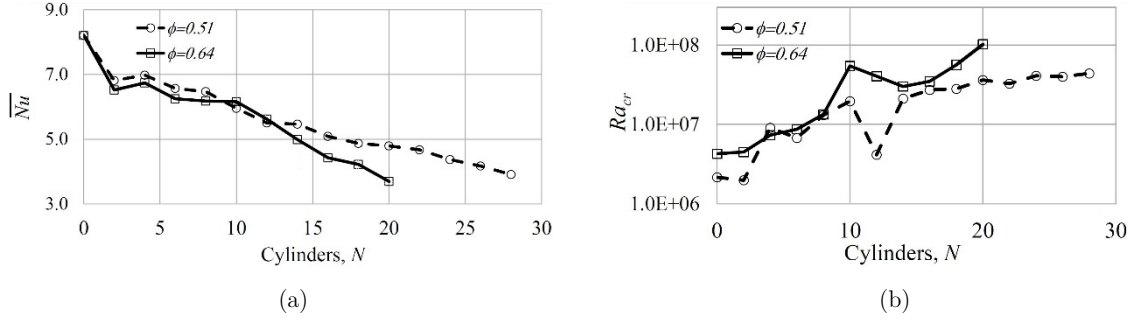


Figure 3.7: Efficiency characteristics of the porous media implants characterized by the minimal ($\phi = 0.51$) and the maximal ($\phi = 0.64$) values of porosity, ϕ , in terms of: (a) \overline{Nu} number, averaged over vertical (hot or cold) boundaries obtained for $Ra_{cr} = 2.15 \times 10^6$, (b) Critical Ra_{cr} number at which the transition from steady to unsteady flow takes place via Hopf bifurcation.

In the next step, the coordinates of the geometric centers of each of the 10 patterns were calculated by taking a weighted average of the positions and the areas of all the voids constituting the corresponding pattern. A further averaging of all the contours confining the obtained patterns and the coordinates of the corresponding geometric centers yielded the averaged shape and position of the two final porous media implants, as shown in Fig. 3.8. In the following, we present the insulating capacity of the constructed implant of porous media characterized by the average porosity value, as well its validation for the realistic 3D flows.

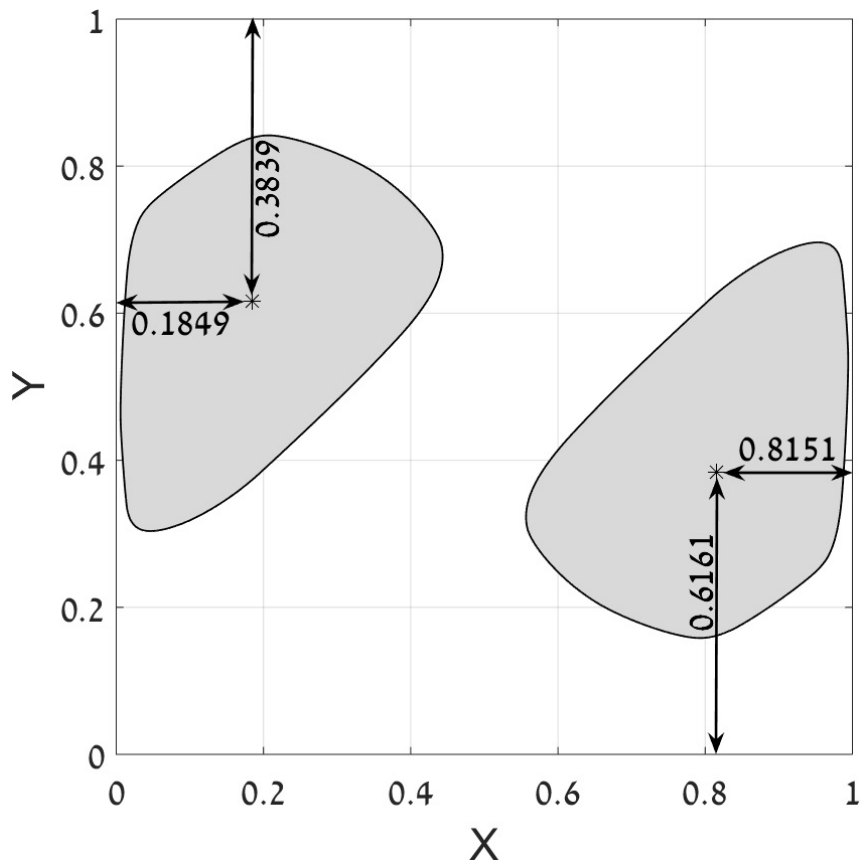
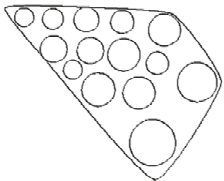
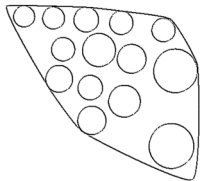
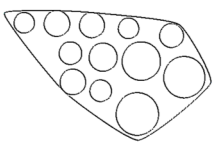
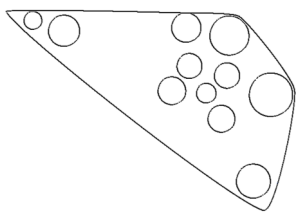
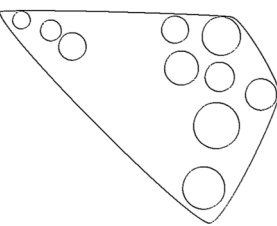
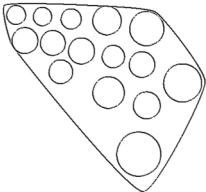
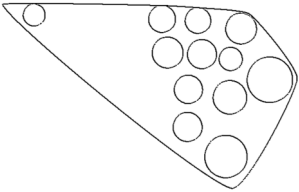
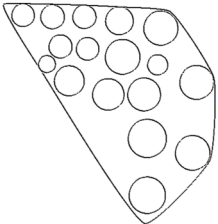


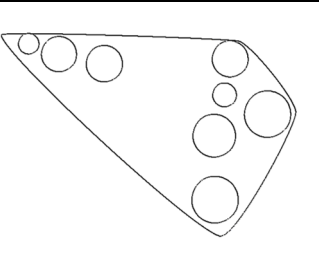
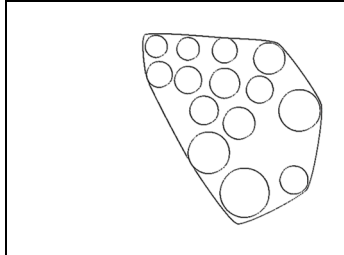
Figure 3.8: Averaged confining contour created using the heterogeneous patterns described above and the coordinate locations representing the center of the contour.

Table 1: Results obtained for the set of 10 different patterns in order of decreasing porosity, ϕ . The patterns are modelled by unconnected packed Beds cylinders of varying diameters, drawn in accordance with a Gaussian distribution characterized by an average value of $D_{av} = 0.1$ and standard deviation of $\sigma = \pm 0.02$.

Trial Number	\overline{Nu} , $Ra = 2.15 \cdot 10^6$	Average Diameter, \overline{D}	\overline{X}_c		\overline{Y}_c		Porosity, ϕ	Shape
			Left	Right	Left	Right		
1	3.9102	0.0715	0.1718	0.8282	0.6116	0.3884	0.5078	
2	4.0799	0.0714	0.1796	0.8204	0.5992	0.4008	0.5239	

3	3.9842	0.0702	0.1413	0.8587	0.5830	0.4170	0.5148	
4	3.8819	0.0726	0.1744	0.8256	0.6448	0.3552	0.5981	
5	3.6968	0.0786	0.2028	0.7972	0.6271	0.3729	0.6388	

6	4.0694	0.0684	0.1732	0.8268	0.6212	0.3788	0.6265	
7	4.0110	0.0766	0.1891	0.8109	0.6289	0.3711	0.6322	
8	3.8609	0.0716	0.2075	0.7925	0.6219	0.3781	0.6222	

9	3.8155	0.0898	0.1962	0.8038	0.6033	0.3967	0.6358	
10	3.9990	0.0770	0.2127	0.7873	0.6202	0.3798	0.6250	

3.2.3 Insulating properties and 3D validation of equi-sized cylinder patterns

We start with constructing the next set of patterns filled with equi-sized cylinders of diameter $D = 0.074$, which is equal to the weighted average of the diameters of all the cylinders involved in the previous set of porous media implants. All the patterns from this set are confined by the contour shown in Fig. 3.8 and are characterized by porosities approximately equal to $\phi \approx 0.5925$, which is the average porosity of all the patterns from the previous set⁷. For all the patterns, the maximal deviation between the target and the actual porosity values did not exceed 5%. The set comprises a special case of a more general configuration, analyzed in the previous section, and aims to address the question of whether the porosity of the modelled porous implant is the dominant parameter determining its insulating capacity. The insulating efficiency of the obtained patterns was next analyzed by calculation of the average \overline{Nu} value for vertical boundaries of the differentially heated cavity at $Ra = 2.15 \times 10^6$. This value corresponds to the value of the critical Ra number for the square differentially heated cavity without obstacles. The obtained results did not reveal a clear trend, indicating that porosity is the only parameter determining the insulating efficiency of the modelled porous implant. In contrast, the maximal and minimal values of the Nusselt number ($\overline{Nu} = 6.3393$ and $\overline{Nu} = 3.9832$, respectively), comprising 77.2% and 48.5% of the \overline{Nu} value obtained for the configuration with no porous implants, were both obtained for the same porosity values (see Fig. 3.9). The high value of the standard deviation, $\sigma = 0.755$, obtained for the set of 10 different patterns also indicates a considerable scattering in the \overline{Nu} values. To further investigate the impact of the cylinder diameter on the thermally insulating capacity of the modelled porous media implant we constructed and simulated 4 more sets (10 patterns per each set) of porous media, each built of equi-sized unconnected

⁷ Note that in the most general case, a precise value of porosity cannot be exactly met by filling up the averaged contour with a discrete number of cylinders

cylinders. The diameter values of the cylinders, one of each set, were $D = 0.04, 0.06, 0.1, 0.16$. All the acquired results were used to obtain the basic statistics for \overline{Nu} values, as summarized in Table 2.

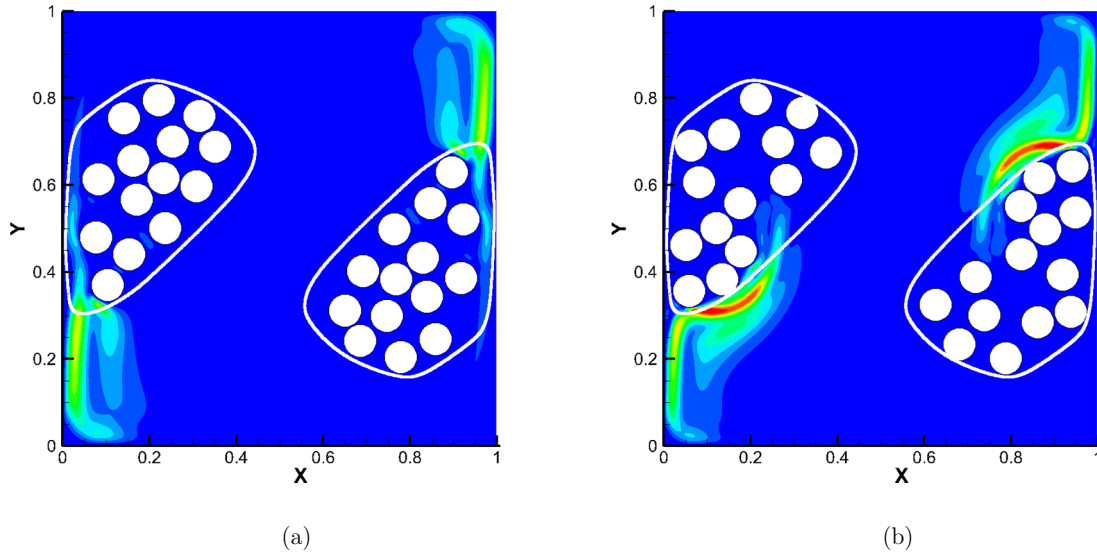


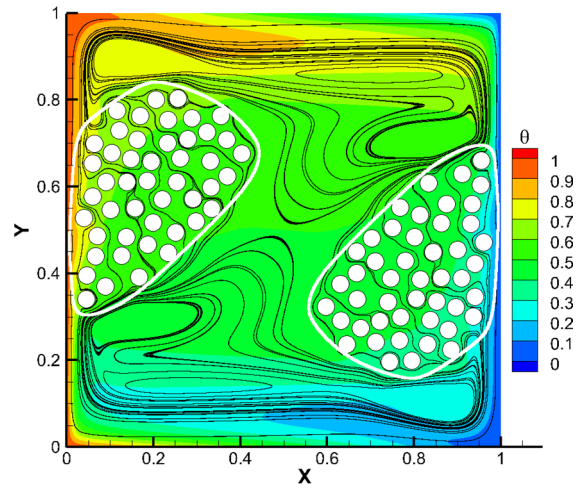
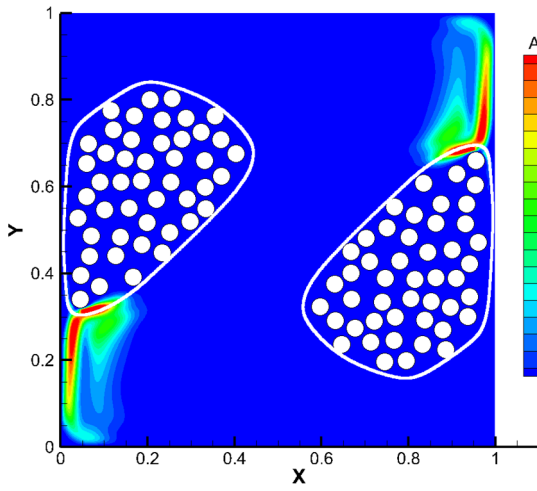
Figure 3.9: Two configurations characterized by approximately the same porosity, $\phi \approx 0.59$, and different thermal insulating capacities: (a) $\overline{Nu}=6.3393$, (b) $\overline{Nu}=3.9832$. All the results are obtained for $Ra = 2.15 \times 10^6$ for differentially heated square cavity.

Table 2: Basic statistics for \overline{Nu} values obtained as a function of the cylinder diameter for each set of the 2D simulations. All of the results were obtained for approximately the same porosity, $\phi \approx 0.59$, for $Ra = 2.15 \times 10^6$.

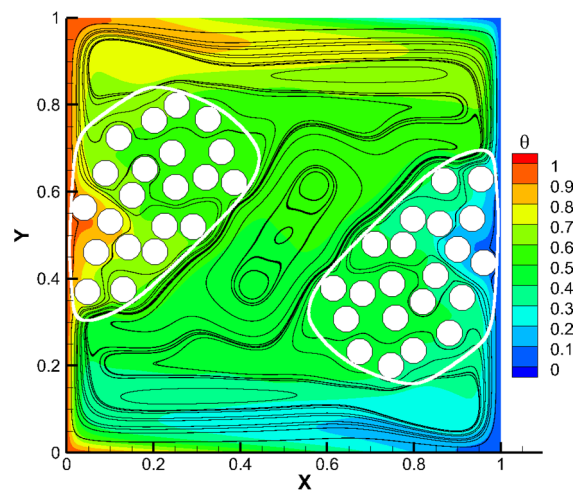
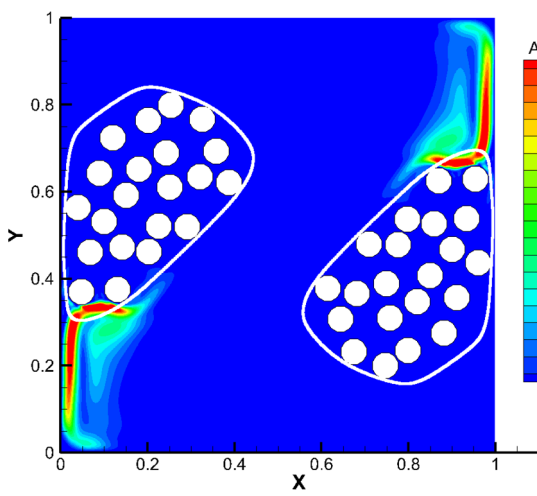
D_{cyl}	N_{cyl}	Nu_{max}	Nu_{min}	\overline{Nu}	σ
0.04	94	3.8086	3.4078	3.5491	0.012
0.06	42	4.4449	3.7187	4.0300	0.105
0.074	28	6.3393	3.9832	4.6759	0.755
0.10	16	7.0326	4.1557	4.9890	0.851
0.16	6	8.0419	3.6894	5.3500	2.004

The porous media implants built of cylinders of smaller diameters exhibit higher insulating capacity, as a result of the decrease in the average values of \overline{Nu} with the cylinder diameter. However, more importantly for increasing the insulating capacity is the rapid decrease in the standard deviation value, σ , which indicates that the porous

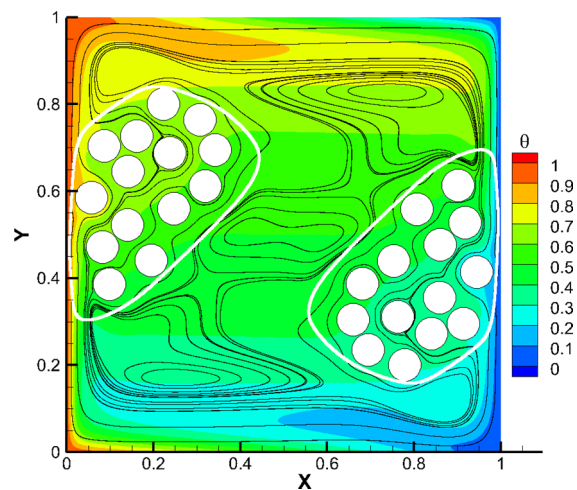
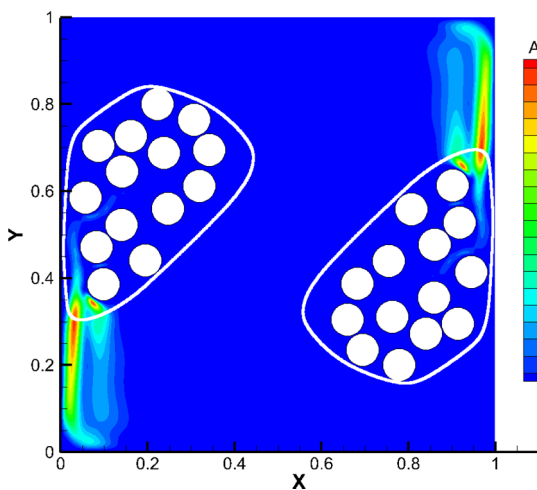
media implants filled with randomly positioned cylinders of smaller diameters are more successful in reproducing the same thermal insulating capacity when compared to the implants consisting of larger cylinders. A physical explanation of the observed phenomenon can be found by looking at contours of optimization parameter \mathbf{A} and the corresponding temperature distributions superimposed by streamlines, obtained for representative porous media patterns (see Fig. 3.10). The patterns shown in Fig. 3.10 have the \overline{Nu} number which is closest to the averaged \overline{Nu} value from the same set. There are no significant differences between the distributions of parameter \mathbf{A} for various patterns (see Fig. 3.10). This is in contrast to the distributions of the flow temperature and streamlines. It can be seen that the implants built of smaller cylinders are uniformly permeable to the convective flow. As the flow infiltrates through the implants it slows down and redistributes evenly. As a result, the temperature distribution inside the implants is almost uniform, which provides their high insulation capacity. On the other hand, the implants built of the larger cylinders are characterized by a non-uniform permeability. In the vicinity of cylindrical obstacles the implants are almost impermeable and only redirect the flow. However, the flow succeeds in penetrating the implants in the outermost regions. Despite decreasing when changing direction, the flow velocity is still high and non-uniform inside a considerable part of the implants. As a result, high values of the temperature gradients are found in these regions, which significantly deteriorates the insulating efficiency of the implants.



(a)



(b)



(c)

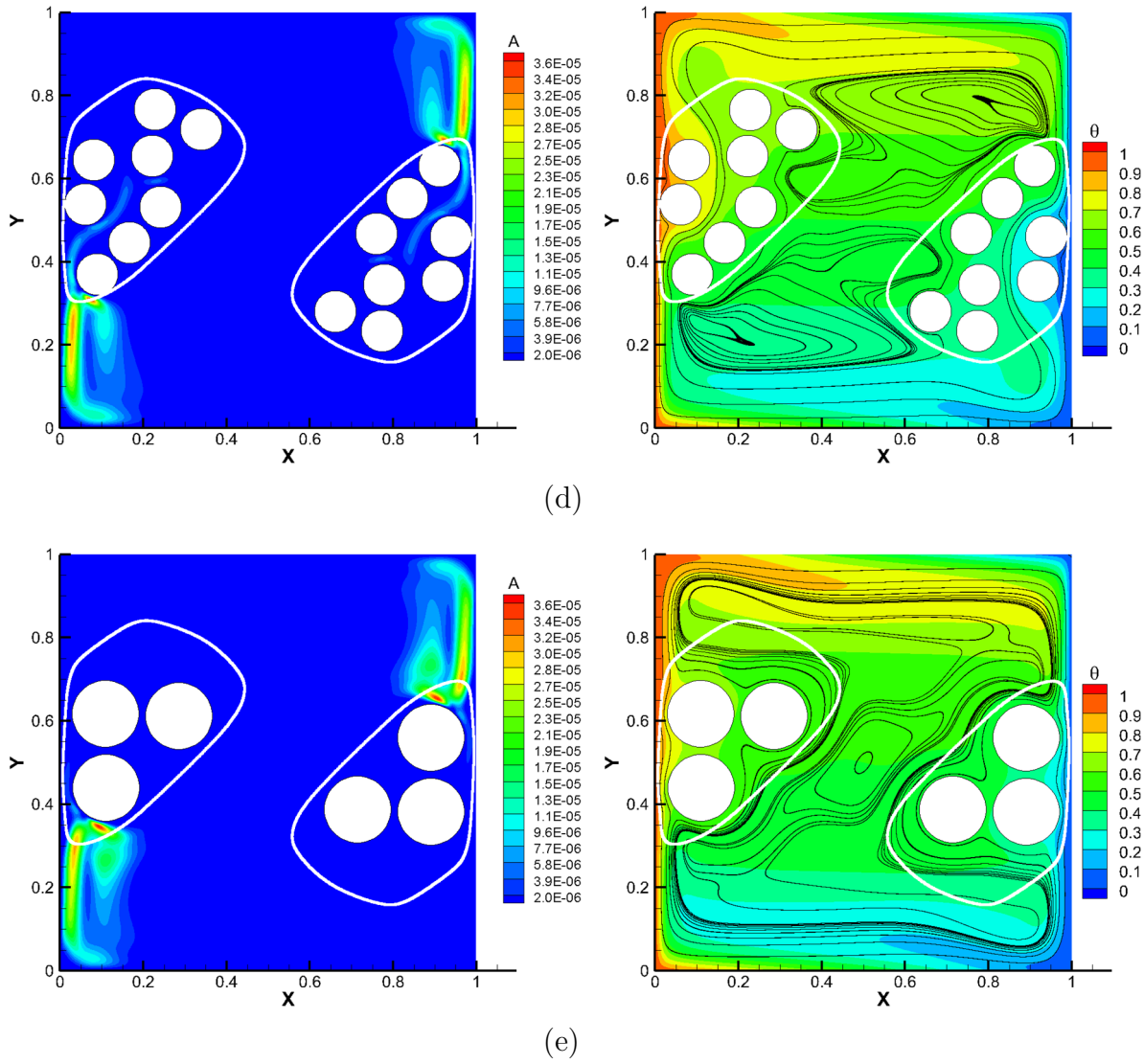


Figure 3.10: Distribution of optimization parameter A (left graphs) and the corresponding temperature field (right graphs) with superimposed streamlines obtained for the implants characterized by approximately the same porosity, $\phi \approx 0.59$, for 2D flow. The implants embedded inside a square differentially heated cavity contain in total: (a) 94 cylinders, (b) 42 cylinders, (c) 28 cylinders, (d) 16 cylinders, (e) 6 cylinders.

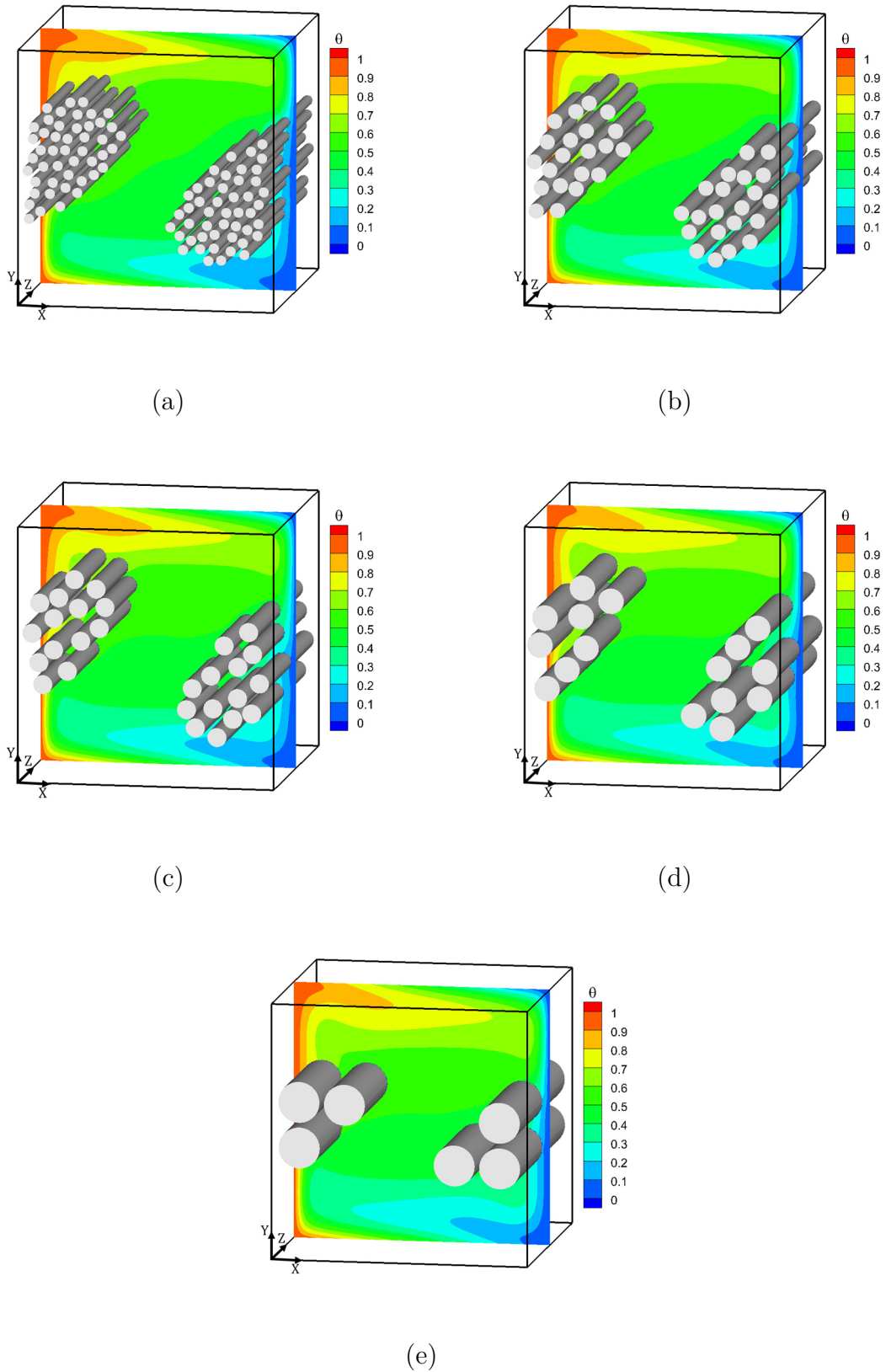


Figure 3.11: Distribution of temperature field in the mid cross section of a 3D cavity obtained for the implants characterized by approximately the same porosity, $\phi \approx 0.59$, for 3D flow. The implants contain in total: (a) 94 cylinders, (b) 42 cylinders, (c) 28 cylinders, (d) 16 cylinders, (e) 6 cylinders.

To validate the observed trends, we performed numerical simulations for realistic 3D flows by extending all the 2D configurations discussed above in the direction normal to the plane of the 2D cavity. As a result, the original 2D configurations are transformed into their 3D analogs (see Fig. 3.11), comprising cubic differentially heated cavities with perfect thermally conducting lateral walls and all non-slip boundaries. The 2D circular obstacles are, in turn, transformed into 3D circular cylinders, extending in a spanwise direction over the entire width of the cavity.

Based on the simulation results, the \overline{Nu} values of all the configurations were then obtained for both 400^3 and 500^3 grid resolutions. Since our method is of second order accuracy, the zero grid size limit for the \overline{Nu} value was estimated by applying the Richardson extrapolation for two consequent grids. All the results are summarized in Table 3.

Table 3: \overline{Nu} values obtained for 400^3 , 500^3 grids and \overline{Nu} value corresponding to the zero grid size limit estimated by the Richardson's extrapolation.

D_{cyl}	N_{cyl}	Nu (grid 400^3)	Nu (grid 500^3)	Nu (Richardson's extrapolation)
0.04	94	4.7727	4.9899	5.3761
0.06	42	5.2666	5.5046	5.9277
0.074	28	5.9388	6.1333	6.4792
0.10	16	5.6794	5.8894	6.2627
0.16	6	6.0119	6.2189	6.5868

It is remarkable that the 3D results demonstrate the same trend that was observed for the 2D simulations: the implants built of smaller cylinders provide better thermal insulation and yield the lower \overline{Nu} values. The \overline{Nu} values continuously rise with an increase in the cylinder diameters. The difference between the maximal and minimal \overline{Nu} values (for approximately the same porosities) for 3D flow is about 22%. This is somewhat lower than the corresponding value obtained for the 2D flow, which is about

50%. The difference stems from the much lower \overline{Nu} value predicted by the 2D simulations for implants built of the cylinders of the smallest diameter, which may be a result of the 2D idealization of the convective flow. Based on the results above, the question that needs answering is: which of the following is the preferable way of suppressing the most unstable flow modes? Is it precise positioning in accordance with the **A** criterion of covering the determined location with clusters of porous material? Further, how important is the impact of the heterogeneity of the porous material?

Recalling that the study addresses the application of the developed method to the thermal insulation of construction blocks⁸, we investigate the sensitivity of the patterns obtained to the opposite temperature difference. In other words, we address the question of whether the thermally insulated construction block will be as efficient in both hot and cold seasons (for both air conditioned and heated indoors) with the enhanced thermal insulation obtained by the proposed method. Table 4 shows the results summarizing the differences in \overline{Nu} values obtained for one of the representative configurations of the porous media implants from each set of 2D configurations and the corresponding 3D analog. No significant differences can be seen for all the cases checked. The deviations do not exceed 10% and 4% for 2D and 3D configurations, respectively. It is remarkable that for both 2D and 3D flows the maximal differences in \overline{Nu} values are observed for implants built of smaller cylinders, which are characterized by the maximal insulation efficiency.

⁸ Calculations regarding the application of this study for a hollow construction block can be found in Appendix B.

Table 4: \overline{Nu} deviation values for the implants described in Table 3 between the presented physical model and the case of vertical wall temperature replacement (implants throughout this study are based on clockwise flow circulation, temperature replacement causes the flow to pass through the existing implants in a counter clockwise circulation inside the cavity) for 2D and 3D.

D_{cyl}	N_{cyl}	Deviation in \overline{Nu} value (2D flow) [%]	Deviation in \overline{Nu} value (3D flow) [%]
0.04	94	9.37	3.34
0.06	42	4.72	3.79
0.074	28	4.78	0.34
0.10	16	3.88	0.40
0.16	6	3.31	0.16

Chapter 4: Summary and Conclusions

The performed study generalized the concept of "smart" thermo-insulating materials built of heterogeneous porous media. In particular, the issue of confined natural convection flow in the presence of heterogeneous porous media was elaborated upon in detail. 2D differentially heated cavities with aspect ratios 8:1 and 1:1 were chosen as testbeds. The obtained 2D results were extensively validated for realistic 3D configurations.

The flow was treated using a mesoscale approach employing the IB method to fully resolve the flow fields in the vicinity of the porous media boundaries. Unconnected packed beds of hollow circular cylinders were used to model the porous media. Basic statistical analysis, encompassing the impact of a whole set of porous media structures consisting of both equi-sized and non-equi-sized cylinders on the insulating efficiency of the porous media implants, was performed. The generalized geometry of the optimized porous media implant and its relative position inside the square differentially heated cavity, comprising a convenient model of the cavity located in the mid-core of construction block, were determined. It may be concluded that:

- The porosity is not the dominant parameter determining the insulating efficiency of the porous implant. Although the explicit determination of the permeability tensor of the porous media implants remained out of the scope of the present study, it was shown that the thermal insulating efficiency of the implants is strongly correlated with their ability to slow down and to uniformly redistribute the infiltrating flow. A more explicit analysis of the permeability of the modelled porous media will be the focus of future work.
- The precise positioning of the cylinders in accordance with the defined optimization parameter \mathbf{A} inside the porous media of a given porosity is not mandatory. The implants modelled by the randomly positioned small size

cylinders exhibit consistent insulating efficiency. On the other hand, it was observed that the variance in the insulating efficiency of the implants increases with the diameter of the cylinders that form the porous media implant modelled by unconnected packed beds.

- The porous media implants modelled by unconnected packed beds of cylinders of smaller diameters are characterized by homogeneous internal patterns and succeed in consistently reproducing the same insulating efficiency. For this reason, among all the available porous materials only those characterized by homogeneous internal patterns should be used when producing the optimized porous media implants.

The results obtained by 2D analysis were extensively validated for realistic 3D flows. The 3D results exhibited the same trends as their 2D analogs, indicating an improvement in insulating efficiency of the implants built of cylinders of the smaller diameter. An acceptable 64% decrease in the \overline{Nu} value was predicted by the 3D analysis of the flow inside the cubic differentially heated cavity with imbedded porous implants, compared to the original non-insulated configuration. It was also verified that the developed "smart" porous media insulation scheme is not sensitive to the opposite temperature difference; thus the insulating efficiency of construction blocks will remain the same in both hot and cold conditions.

Appendix A: De Casteljau Bézier curve

A De Casteljau Bézier curve is a spline method in linear algebra used in digital graphics, among other related fields, in order to create a smooth shape using a series of points.

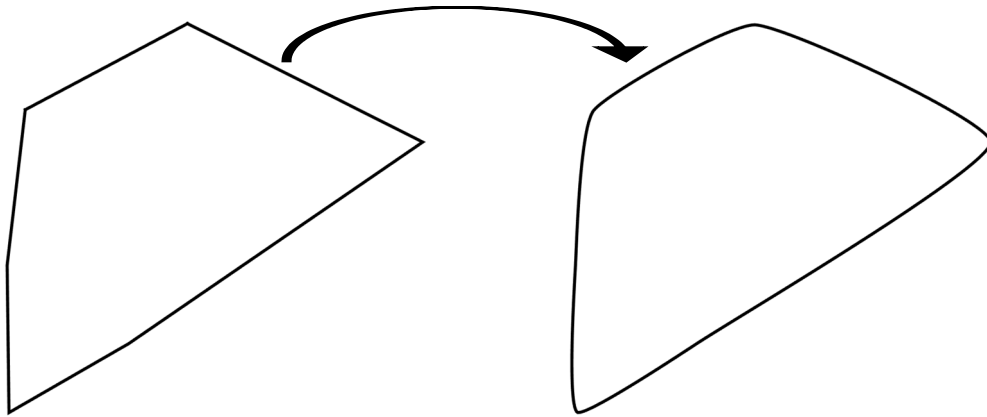


Figure A.1: Smoothing sharp-edged polygon using De Casteljau Bézier method.

A De Casteljau Bézier curve basis is a linear connection between two coordinates, P_0 and P_1 , while the coordinate Q_0 is the convex combination of the two points. Its position along the line connecting P_0 and P_1 depends on the parameter t , which varies from 0 to 1 according to the function it represents (in our research, the parameter t varies linearly from 0 to 1. Note that Q_0 can be positioned before P_0 and after P_1 by setting t to be less than zero or higher than one, respectively). The function which represents Q_0 can be written as:

$$Q_0(t) \equiv (1-t)P_0 + tP_1 \tag{A.1}$$

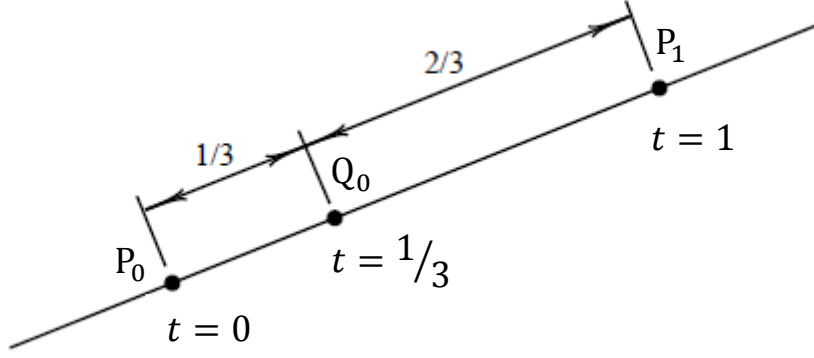


Figure A.2: Q_0 is a convex combination of P_0 and P_1 , depending on the parameter t ; example of a case where $t=1/3$ [49].

A De Casteljaou Bézier parabolic curve is also called a Bézier quadratic curve and it depends on three coordinates, P_0, P_1 and P_2 so that there are two convex points, one on the line $P_0 - P_1$ and the other on the line $P_1 - P_2$, Q_0 and Q_1 , respectively.

$$Q_0(t) \equiv (1-t)P_0 + tP_1 \quad (\text{A.2})$$

$$Q_1(t) \equiv (1-t)P_1 + tP_2 \quad (\text{A.3})$$

The two convex points travel along the lines, both depending on the parameter t (as t increases, Q_0 departs from P_0 and moves towards P_1 , and Q_1 departs from P_1 and moves towards P_2 , see Fig. A.3-b), and another point can be extracted using a convex combination between the two new points (Q_0 and Q_1) - R_0 , which will also travel along the $Q_0 - Q_1$ line (as a function of t). The function which represents R_0 can be written as:

$$R_0(t) \equiv (1-t)Q_0 + tQ_1 \quad (\text{A.4})$$

Combining the three equations, Eqs (A.2), (A.3) and (A.4), we get that $R_0(t)$ is a convex combination of P_0, P_1 and P_2 . Note that the curve $R_0(t)$ is made of points tangent to the line $Q_0 - Q_1$ (Fig. A.3-a):

$$R_0(t) = (1-t)^2 P_0 + 2(1-t)tP_1 + t^2 P_2 \quad (\text{A.5})$$

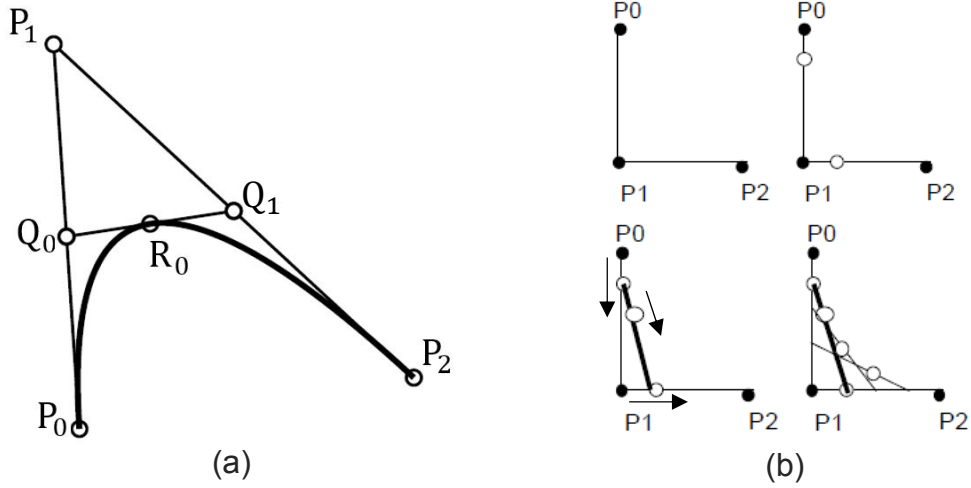


Figure A.3: (a) Example of an arc where $t=1/2$, (b) Illustration of how the points Q_0 , Q_1 and R_0 advance as t increases from 0 to 1 while R_0 draws the curve [49] and [50].

It can be noted that the coefficients within the convex equations act according to the binomial theorem so that we can write the generalized formulation:

$$P(t) = \sum_{i=0}^n \binom{n}{i} (1-t)^{n-i} t^i P_i \quad (\text{A.6})$$

while it is known in the binomial theorem that:

$$\binom{n}{i} = \frac{n!}{i!(n-i)!} \quad (\text{A.7})$$

As shown in Fig. A.3-a the curve between P_0 and P_2 is created by following point R_0 while t goes from 0 to 1. The curve does not go through P_1 , but this point is highly significant and it determines how the curve will be tangential at points P_0 and P_2 ; the significance of the point will be further discussed in the following.

Applying Eq. (A.6) with a third linear interpolation gives the cubic Bézier (a curve which relies on 4 points):

$$S_0(t) = (1-t)^3 P_0(t) + 3(1-t)^2 t P_1(t) + 3(1-t) t^2 P_2(t) + t^3 P_3(t) \quad (\text{A.8})$$

As written before, Fig. A.4-a presents a curve that does not intersect points P_1 and P_2 , but those points will nevertheless define the behavior of the curve, so it can be concluded that the position of the coordinates P_1 and P_2 effects the curve's behavior, while the

coordinates P_0 and P_3 are the points at which the curve is tangent. P_0 and P_3 can be seen as the “anchors” and P_1 and P_2 as the “control points”. Fig. A.4-b demonstrates the difference between two curves depending on the “anchor” points and the “control” points. As mentioned earlier, another way to control the orientation of the curve is to define the parameter t to be a deferent function between two adjacent polygon points so that the convex combination will go from 0 to 1 at a different rate compared to another convex point.

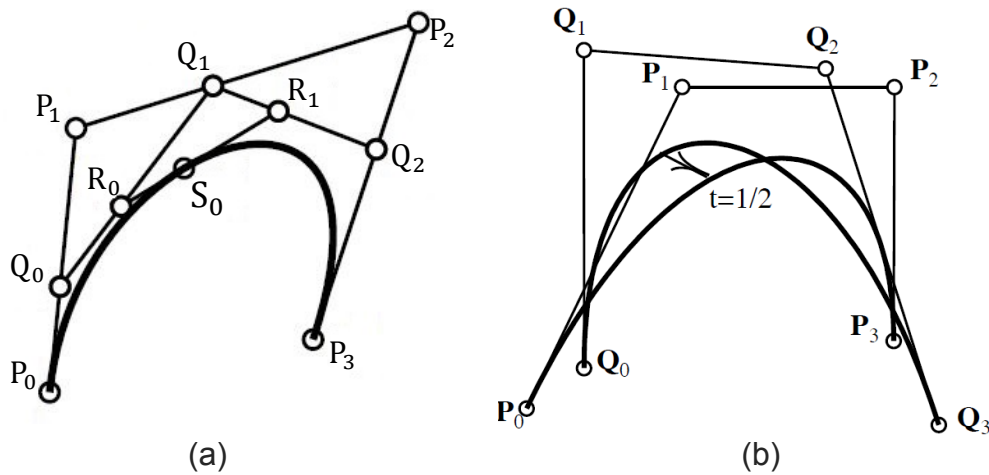


Figure A.4: Cubic Bézier: (a) s_0 defines the curve using the anchors and the control points, (b) The effects of the control points on the curve [49].

A De Casteljau Bézier curve can use more points to further increase the flexibility in the orientation of the curve. In the present study only the cubic De Casteljau Bézier curve was utilized. Using cubic De Casteljau Bézier curves it is possible to smoothe different polygons to newly defined forms by defining every two adjacent coordinates of the polygon to be anchors of a curve drawn between them. In order to use the method, two control points have to be created to define the curve; using an algorithm developed in [51] we can create control points and scale them to adjust the curve according to the predefined constraints. Figure A.5 describes the process of determining the control points. First, the middle points of each edge of the polygon must be found (A_i) and then, using the line segments (C_i), the middle points are connected. The locations of points (B_i) on the line segments (C_i) are proportional to the ratio of the length of the polygon edges upon which the middle points are located. For example, the location of a point on

the left line segment splits the segment ($d1$ and $d2$) in the same ratio as $L1$ related to $L2$ (see Fig. A.5b). The final step of creating the control points is described in Fig. A.5c. Each point (B_i) shifts along the line segment to the corresponding vertex, so that the line's segment orientation remains untouched. As a result, all of the polygon's vertices (anchors) and their control points are gained together.

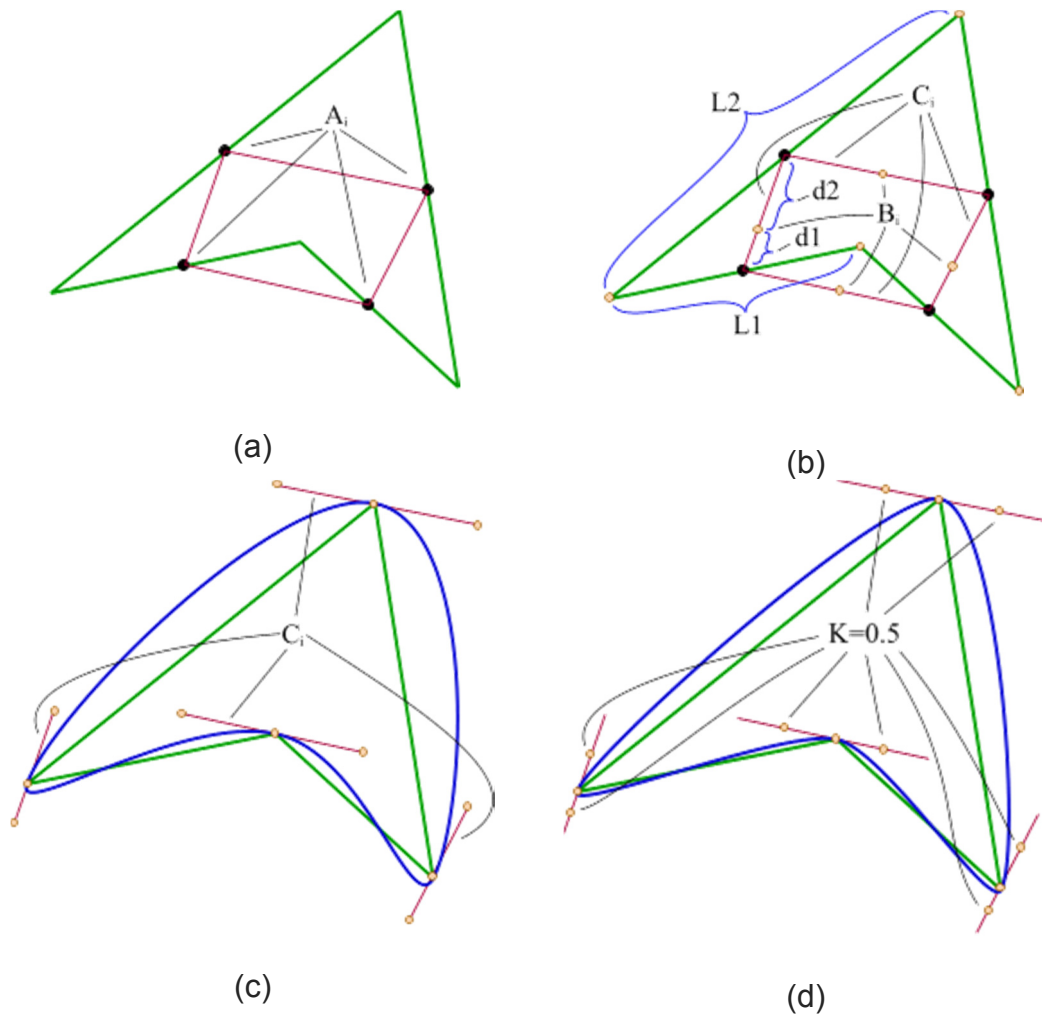


Figure A.2: Steps used by Maxim [51] in order to find the optimal control points which will best represent the polygon.

In order to adjust the overall shape of the resulting curves, the control points can be moved along the line connecting it to the corresponding anchor point by using the multiplication factor K (see Fig. A.5-d that visualizes the described procedure). In the present study, the 0.3 value was assigned to the multiplier K to empirically generate the

smooth closed curve determining the external boundaries of the implant of the modelled porous media.

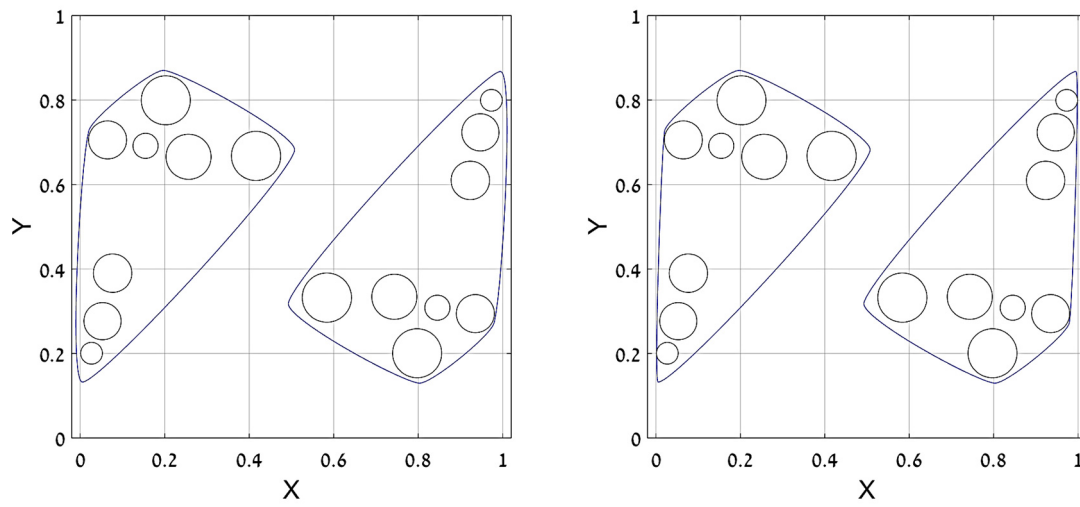


Figure A.3: From left to right, Bezier curve made with 0.5 smoothing value and 0.3 smoothing value.

Appendix B: Estimation of dimensions of realistic hollow construction blocks

Recalling that the above study was performed on the basis of non-dimensional analysis, it would be of practical interest to estimate the dimensions of realistic construction blocks to which the developed method of “smart” thermal insulation could be applied. Without loss of generality we will assume that the cavity located in the mid-core of a construction block is of cubic geometry. We will next estimate the range of the length of the cavity edge, L , for the given range of temperature difference, $20[K] \leq \Delta T < 40[K]$, between the indoor and the outdoor environment. Note that the final dimensions of the construction block, including the wall and the bottom thicknesses, should account for features inherent to technological processes and comply with the requirements imposed on the strength of the block and, therefore, should be further determined by the manufacturer.

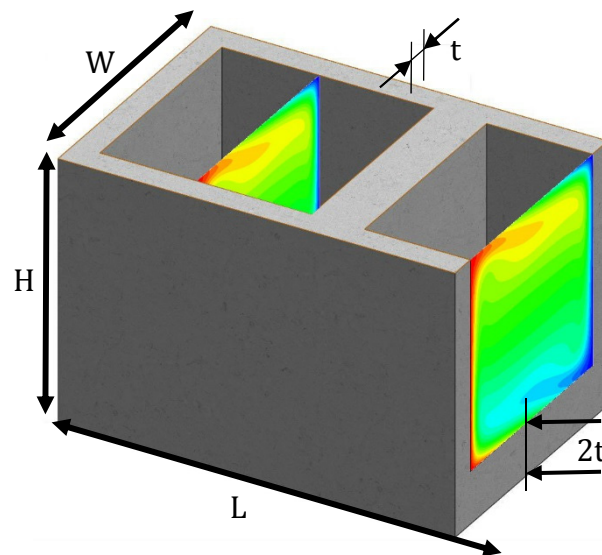


Figure B.1: Cross section of a hollowed block ($W \times H \times L$) with t as its wall thickness.

The expression for the length x can be obtained from the definition of the Ra number as $x = \sqrt[3]{\frac{Ra \cdot \nu \alpha}{g \beta \Delta T}}$, where $x = H - 2t$. The physical properties of dry air at $T =$

300[K] indicate the values of $\nu = 1.568 \times 10^{-5} \left[\frac{m^2}{sec} \right]$, $\alpha = 22.07 \times 10^{-6} \left[\frac{m^2}{sec} \right]$, $\beta = \frac{1}{T} \left[\frac{1}{K} \right]$.

We next recall that the non-dimensional analysis was performed for the value of $Ra = \frac{g\beta}{\nu\alpha} \Delta T L^3 = 2.15 \times 10^6$ and that the value of gravitational acceleration \mathbf{g} is equal to $g = 9.81 \left[\frac{m}{sec^2} \right]$. Substitution of all the above values into the expression for x yields the characteristic dimensions of $x \approx 0.1[m]$ for $\Delta T = 20[K]$ and $x \approx 0.08[m]$ for $\Delta T = 40[K]$, which are typical of realistic construction blocks.

Appendix C: Deriving the dimensionless equations of motion

In chapter 2 the governing equations for the incompressible buoyancy driven flow are presented:

$$\nabla \cdot \mathbf{u} = 0 \quad (\text{C.1})$$

$$\rho \left(\frac{\partial \mathbf{u}}{\partial t} + (\mathbf{u} \cdot \nabla) \mathbf{u} \right) = -\nabla p + \mu \nabla^2 \mathbf{u} + \rho \mathbf{g} \quad (\text{C.2})$$

$$\frac{\partial T}{\partial t} + (\mathbf{u} \cdot \nabla) T = \alpha \nabla^2 T \quad (\text{C.3})$$

After utilizing the assumptions mentioned in chapter 2, the momentum equation can be rewritten:

$$\rho_0 \left(\frac{\partial \mathbf{u}}{\partial t} + (\mathbf{u} \cdot \nabla) \mathbf{u} \right) = -\nabla p + \mu \nabla^2 \mathbf{u} + \rho_0 (1 - \beta(T - T_C)) \mathbf{g} \quad (\text{C.4})$$

At the next step, a new definition of the pressure is introduced, which includes both the hydrodynamic and hydrostatic pressure components, reading $\bar{P} = p + \rho_0 g y$, so that in the equation $\nabla \bar{P} = \nabla p + \rho_0 \mathbf{g}$ (the gravity acts in the negative direction of the y axis). The momentum equation can be rewritten as:

$$\rho_0 \left(\frac{\partial \mathbf{u}}{\partial t} + (\mathbf{u} \cdot \nabla) \mathbf{u} \right) = -\nabla \bar{P} + \mu \nabla^2 \mathbf{u} - \rho_0 \mathbf{g} \beta (T - T_C) \quad (\text{C.5})$$

The generalization of the problem was made by introducing characteristic scales for the length \mathbf{x} , velocity \mathbf{u} , time t , pressure p and temperature T fields as follows:

$$U = \sqrt{g \beta L \Delta T} ; t_0 = \frac{L}{U} ; P = \rho_0 U^2 ; \Delta T = T_H - T_C ; Ra = \frac{g \beta}{\nu \alpha} \Delta T L^3 ; Pr = \frac{\nu}{\alpha}$$

where \mathbf{g} is the gravitational acceleration, β is adiabatic coefficient of thermal expansion, L is the length of the square differentially heated cavity, ΔT is the temperature difference

between the hottest and coldest boundaries and ρ is the mass density of the working fluid. Ra and Pr are the Rayleigh and Prandtl numbers, where α is the thermal diffusivity and ν is the kinematic viscosity.

The dimensional variables of the problem can then be normalized as:

$$\mathbf{x}^* = \frac{\mathbf{x}}{L} ; \mathbf{u}^* = \frac{\mathbf{u}}{U} ; t^* = \frac{t}{t_0} ; \bar{P}^* = \frac{\bar{P}}{P} ; \theta = \frac{T - T_C}{T_H - T_C} ; T^* = \frac{T}{T_0}$$

Continuity equation:

Using the above normalization, the continuity equation (C.1) yields:

$$\frac{U}{L} \nabla^* \cdot \mathbf{u}^* = 0 \Rightarrow \nabla^* \cdot \mathbf{u}^* = 0 \quad (\text{C.6})$$

Momentum equation:

Dividing Eq. (C.5) by ρ_0 yields:

$$\frac{\partial \mathbf{u}}{\partial t} + (\mathbf{u} \cdot \nabla) \mathbf{u} = -\frac{\nabla \bar{P}}{\rho_0} + \nu \nabla^2 \mathbf{u} - \mathbf{g} \beta (T - T_C)$$

Utilizing the normalization parameters gives:

$$\frac{U^2}{L} \frac{\partial \mathbf{u}^*}{\partial t^*} + \frac{U^2}{L} (\mathbf{u}^* \cdot \nabla^*) \mathbf{u}^* = -\frac{\nabla^* \overline{\rho_0 U^2 P^*}}{L \rho_0} + \frac{U}{L^2} \nu \nabla^{*2} \mathbf{u}^* - \mathbf{g} \beta (T - T_C)$$

Dividing the equation by $\frac{U^2}{L}$ and rearranging, it can be rewritten as:

$$\frac{\partial \mathbf{u}^*}{\partial t^*} + (\mathbf{u}^* \cdot \nabla^*) \mathbf{u}^* = -\nabla^* \bar{P}^* + \frac{\nu}{LU} \nabla^{*2} \mathbf{u}^* + \frac{\mathbf{g} \beta (T - T_C) L}{U^2} \mathbf{e}_y$$

Plugging the characteristic parameters into the equation yields:

$$\frac{\partial \mathbf{u}^*}{\partial t^*} + (\mathbf{u}^* \cdot \nabla^*) \mathbf{u}^* = -\nabla^* \bar{P}^* + \frac{\nu}{L \sqrt{\mathbf{g} \beta \Delta T L}} \nabla^{*2} \mathbf{u}^* + \frac{\mathbf{g} \beta (T - T_C) L}{\mathbf{g} \beta \Delta T L} \mathbf{e}_y \quad (\text{C.7})$$

By rearranging the coefficient of $\bar{\mathbf{e}}_y$, it is noticeable that only t θ remain, and, by looking at the coefficients of $\nabla^{*2} \mathbf{u}^2$ and the definition of the dimensionless numbers Pr and Ra , it follows that:

$$\frac{\nu}{L\sqrt{g\beta\Delta TL}} = \sqrt{\frac{Pr}{Ra}}$$

Hence, the non-dimensional momentum equation can be written as:

$$\frac{\partial \mathbf{u}^*}{\partial t^*} + (\mathbf{u}^* \cdot \nabla^*) \mathbf{u}^* = -\nabla^* \overline{P^*} + \sqrt{\frac{Pr}{Ra}} \nabla^{*2} \mathbf{u}^* + \theta \overline{e}_y \quad (\text{C.8})$$

Energy equation:

Eq. (C.3) rewritten in terms of non-dimensional parameters reads:

$$\frac{UT_0}{L} \frac{\partial T^*}{\partial t^*} + \frac{UT_0}{L} (\mathbf{u}^* \cdot \nabla^*) T^* = \frac{T_0}{L^2} \alpha \nabla^{*2} T^* \quad (\text{C.9})$$

Dividing equation (C.9) by $\frac{UT_0}{L}$ and using $\theta = \frac{T-T_C}{T_H-T_C}$ as non-dimensional temperature yields:

$$\frac{\partial \theta^*}{\partial t^*} + (\mathbf{u}^* \cdot \nabla^*) \theta^* = \frac{\alpha}{LU} \nabla^{*2} \theta^*$$

Plugging the characteristic parameters into the equation:

$$\frac{\partial \theta^*}{\partial t^*} + (\mathbf{u}^* \cdot \nabla^*) \theta^* = \frac{\alpha}{L\sqrt{g\beta\Delta TL}} \nabla^{*2} \theta^* \quad (\text{C.10})$$

By looking at the coefficients of $\nabla^{*2} \theta$ and the definition of non-dimensional numbers Pr and Ra it can be seen that:

$$\frac{\alpha}{L\sqrt{g\beta\Delta TL}} = \frac{1}{\sqrt{Pr \cdot Ra}}$$

Hence, the non-dimensional momentum equation reads:

$$\frac{\partial \theta^*}{\partial t^*} + (\mathbf{u}^* \cdot \nabla^*) \theta^* = \frac{1}{\sqrt{Pr \cdot Ra}} \nabla^{*2} \theta^* \quad (\text{C.11})$$

For the sake of simplicity, the stars attached to non-dimensional parameters are omitted yielding the following normalized system of the governing equations:

$$\nabla \cdot \mathbf{u} = 0 \quad (\text{C.12})$$

$$\frac{\partial \mathbf{u}}{\partial t} + (\mathbf{u} \cdot \nabla) \mathbf{u} = -\nabla p + \sqrt{\frac{Pr}{Ra}} \nabla^2 \mathbf{u} + \theta \bar{e}_y \quad (\text{C.13})$$

$$\frac{\partial \theta}{\partial t} + (\mathbf{u} \cdot \nabla) \theta = \frac{1}{\sqrt{PrRa}} \nabla^2 \theta \quad (\text{C.14})$$

References

- [1] C. A. Balaras, K. Droutsas, A. A. Argiriou and D. N. Asimakopoulos, "Potential for energy conservation in apartment buildings," *Energy and Buildings*, vol. 32, no. 2, pp. 143-154, 1999.
- [2] Y. Feng, "Thermal design standards for energy efficiency of residential buildings in hot summer/cold winter zones," *Energy and Buildings*, vol. 36, no. 12, pp. 1309-1312, 2004.
- [3] M. Ciampi, F. Leccese and G. Tuoni, "Ventilated facades energy performance in summer cooling of buildings.," *Solar Energy*, vol. 75, no. 6, pp. 491-502, 2003.
- [4] L. M. Al-Hadhrami and A. Ahmad., "Assessment of thermal performance of different types of masonry bricks used in Saudi Arabia.," *Applied thermal engineering*, vol. 29, no. 5, pp. 1123-1130, 2009.
- [5] T. Shimizu, K. Matsuura, H. Furue and K. Matsuzak, "Thermal conductivity of high porosity alumina refractory bricks made by a slurry gelation and foaming method.," *Journal of the European ceramic Society*, vol. 33, no. 15, pp. 3249-3435, 2013.
- [6] S. Mucahit and S. Akkurt, "The use of recycled paper processing residues in making porous brick with reduced thermal conductivity.," *Ceramics International*, vol. 35, no. 7, pp. 2625-2631, 2009.
- [7] M. A. Antar, "Thermal radiation role in conjugate heat transfer across a multiple-cavity building block.," *Energy*, vol. 35, no. 8, pp. 3508-3516, 2010.
- [8] S. Mucahit, J. José del Coz Díaz, F. P. Á. Rabanal, O. Gencel and S. Akkurt, "Thermal performance optimization of hollow clay bricks made up of paper waste," *Energy and Buildings*, vol. 75, pp. 96-108, 2014.
- [9] T. W. Tong and F. M. Gerner, "Natural convection in partitioned air-filled rectangular enclosures.," *International communications in heat and mass transfer*, vol. 13, no. 1, pp. 99-108, 1986.
- [10] A. Kangni, R. B. Yedder and E. Bilgen, "Natural convection and conduction in enclosures with multiple vertical partitions.," *International journal of heat and mass transfer*, vol. 34, no. 11, pp. 2819-2825, 1991.
- [11] V. A. F. Costa, "Improving the thermal performance of red clay holed bricks.," *Energy and Buildings*, vol. 70, pp. 352-364, 2014.

- [12] B. Ammar, "Steady state theoretical model of fired clay hollow bricks for enhanced external wall thermal insulation," *Building and Environment*, vol. 43, no. 10, pp. 1603-1618, 2008.
- [13] J. J. del Coz Díaz, P. G. Nieto, J. S. Sierra and C. B. Biempica, "Nonlinear thermal optimization of external light concrete multi-holed brick walls by the finite element method.," *International Journal of Heat and Mass Transfer*, vol. 51, no. 7, pp. 1530-1541, 2008.
- [14] J. J. del Coz Díaz, P. G. Nieto, J. S. Sierra and I. P. Sánchez, "Non-linear thermal optimization and design improvement of a new internal light concrete multi-holed brick walls by FEM.," *Applied Thermal Engineering*, vol. 28, no. 8, pp. 1090-1100, 2008.
- [15] J. J. del Coz Díaz, P. G. Nieto, J. D. Hernández and A. S. Sánchez, "Thermal design optimization of lightweight concrete blocks for internal one-way spanning slabs floors by FEM.," *Energy and Buildings*, vol. 41, no. 12, pp. 1276-1287, 2009.
- [16] L. Li, Z. Wu, Z. Li, Y. He and W. Tao, "Numerical thermal optimization of the configuration of multi-holed clay bricks used for constructing building walls by the finite volume method.," *International Journal of Heat and Mass Transfer*, vol. 51, no. 13, pp. 3669-3682, 2008.
- [17] M. A. Antar and B. Hasan, "Conjugate conduction-natural convection heat transfer in a hollow building block.," *Applied Thermal Engineering*, vol. 29, no. 17, pp. 3716-3720, 2009.
- [18] Y. Varol, O. F. Hakan and P. Loan, "Natural convection in a diagonally divided square cavity filled with a porous medium.," *International Journal of Thermal Sciences*, vol. 48, no. 7, pp. 1405-1415, 2009.
- [19] M. M. Alhazmy, "Numerical investigation on using inclined partitions to reduce natural convection inside the cavities of hollow bricks.," *International Journal of Thermal Sciences*, vol. 49, no. 11, pp. 2201-2210, 2010.
- [20] M. M. AlHazmy, "Analysis of coupled natural convection-conduction effects on the heat transport through hollow building blocks.," *Energy and Buildings*, vol. 38, no. 5, pp. 515-521, 2006.
- [21] D. Tang, L. Li, C. Song, W. Tao and Y. He, "Numerical Thermal Analysis of Applying Insulation Material to Holes in Hollow Brick Walls by the Finite-Volume Method.," *International Journal of Computation and Methodology*, vol. 68, no. 5, pp. 526-547, 2015.
- [22] E. Bilgen, "Natural convection in enclosures with partial.," *Renewable Energy*, vol. 26, no. 2, pp. 257-270, 2002.

- [23] A. A. Merrikh and L. J. L., "Natural convection in an enclosure with disconnected and conducting solid blocks.," *International Journal of Heat and Mass Transfer*, vol. 48, no. 7, pp. 1361-1372, 2005.
- [24] E. J. Braga and M. J. d. Lemos., "Laminar natural convection in cavities filled with circular and square rods.," *International Communications in Heat and Mass Transfer*, vol. 32, no. 10, pp. 1289-1297, 2005.
- [25] E. J. Braga and J. D. L. Marcelo, "Heat transfer in enclosures having a fixed amount of solid material simulated with heterogeneous and homogeneous models."
- [26] O. Laguerre, S. Benamara, D. Remy and D. Flick, "Experimental and numerical study of heat and moisture transfers by natural convection in a cavity filled with solid obstacles.," *International Journal of Heat and Mass Transfer*, vol. 52, no. 25, pp. 5691-5700, 2009.
- [27] S. Jamalud-Din, D. Rees, B. Reddy and A. Narasimhan, "Prediction of natural convection flow using network model and numerical simulations inside enclosure with distributed solid blocks.," *Heat and mass transfer*, vol. 46, no. 3, pp. 333-343, 2010.
- [28] S. Junqueira, F. D. Lai, A. Franco and J. Lage, "Numerical Investigation of Natural Convection in Heterogeneous Rectangular Enclosures.," *Heat Transfer Engineering*, vol. 64, no. 5-6, pp. 460-469, 2013.
- [29] D. Iyi and H. Reaz, "Natural Convection Flow and Heat Transfer in an Enclosure Containing Staggered Arrangement of Blockages.," *Procedia Engineering*, vol. 105, pp. 176-183, 2015.
- [30] D. J. Braga and M. J. d. Lemos, "Laminar natural convection in cavities filled with circular and square rods.," *International Communications in Heat and Mass Transfer*, vol. 32, no. 10, pp. 1289-1297, 2005.
- [31] K. Vafai and C. L. Tien, "Boundary and inertia effects on flow and heat transfer in porous media.," *International Journal of Heat and Mass Transfer*, vol. 24, no. 2, pp. 195-203, 1981.
- [32] R. A. Silva and M. J. de Lemos, "Turbulent flow in a channel occupied by a porous layer considering the stress jump at the interface.," *International Journal of Heat and Mass Transfer*, vol. 46, no. 26, pp. 5113-5121, 2003.
- [33] Y. Gulbeg, Immersed boundary method for investigation of confined thermally driven flow., M. S. Thesis, Ed., Department of Mechanical Engineering: Ben Gurion University of the Negev, Be'er-Sheva, 2016.

- [34] Y. Feldman and Y. Gulbeg, "A fully pressure-velocity coupled immersed boundary method based on the Lagrange multiplier approach," *Journal of Computational Physics*, 2015.
- [35] Y. Gulbeg and Y. Feldman, "Flow control through use of heterogeneous porous media: Smart passive thermo-insulating materials," *International Journal of Thermal Sciences*, vol. 110, pp. 369-382, 2016.
- [36] S. V. Patankar, "Numerical heat transfer and fluid flow: Computational methods in mechanics and thermal science.," *McGraw-Hill*, 1980.
- [37] A. Y. Gelfgat, "Three-dimensional instability of axisymmetric flows: solution of benchmark problems by a low-order finite volume method.," *International journal for numerical methods in fluids*, vol. 54, no. 3, pp. 269-294, 2007.
- [38] Y. Feldamn and A. Gelfgat, "On pressure-velocity coupled time-integration of incompressible Navier-Stokes equations using direct inversion of Stokes operator or accelerated multigrid technique," *Computers and Structures*, vol. 87, pp. 710-720, 2009.
- [39] C. Peskin, "Flow patterns around heart valves: a numerical method," *Journal of Computational physics*, vol. 10, pp. 252-271, 1972.
- [40] K. Taira and T. Colonius, "The immersed boundary method: A projection approach," *Journal of Computational physics*, vol. 225, pp. 3121-3133, 2007.
- [41] A. M. Roma, C. S. Peskin and M. J. Berger, "An adaptive version of the immersed boundary method.," *Journal of computational physics*, vol. 153, pp. 509-534, 1999.
- [42] H. Vitoshkin and A. Gelfgat, "On direct inverse of Stokes, Helmholtz and Laplacian operators in view of time-stepper-based Newton and Arnoldi solvers in incompressible CFD," *Commun. Comput. Phys*, vol. 14, pp. 1103-1119, 2013.
- [43] M. Uhlmann, "An immersed boundary method with direct forcing for the simulation of particulate flows," *Journal of Computational Physics*, vol. 209, pp. 448-476, 2005.
- [44] L. S. X. a. J. W. Demmel, "SuperLU_DIST: A scalable distributed-memory sparse direct solver for unsymmetric linear systems.," *ACM Transactions on Mathematical Software (TOMS)*, vol. 29, pp. 110-140, 2003.
- [45] A. Gelfgat, "Stability of convective flows in cavities: solution of benchmark problems by a low-order finite volume method," *International Journal for Numerical Methods in Fluids*, vol. 53, pp. 485-506, 2006.

- [46] T. Kempe and F. Jochen, "An improved immersed boundary method with direct forcing for the simulation of particle laden flows," *Journal of Computational Physics*, vol. 231, no. 9, pp. 3663-3684, 2012.
- [47] A. Gelfgat, "Oscillatory instability of three-dimensional natural convection of air in a laterally heated cubic box," *arXiv:1508.00652*, 2015.
- [48] Y. Gulbeg and Y. Feldman, "On laminar natural convection inside multi-layered," *Int. J. Heat and Mass Transfer*, vol. 91, pp. 908-921, 2015.
- [49] W. T. Sederberg, *Computer Aided Geometric Design Course Notes*, Brigham: BYU, 2014.
- [50] J. Dill, "The de Casteljau Algorithm for Evaluating Bezier Curves," 29 October 2000. [Online]. Available: https://www.pedagogie.ac-aix-marseille.fr/upload/docs/application/pdf/2012-02/decasteljau_john.pdf.
- [51] M. Shermanarev, "AntiGrain," 8 July 2007. [Online]. Available: www.AntiGrain.com.
- [52] W. W. Ren, C. Shu and J. W. & W. M. Yang, "Boundary condition-enforced immersed boundary method for thermal flow problems with Dirichlet temperature condition and its applications.," *Computers & Fluids*, vol. 57, pp. 40-51, 2012.
- [53] M. Lappa, *Thermal Convection: Patterns, Evolution and Stability*, Chichester: John Wiley & Sons, 2010.
- [54] A. A. Merrikh and J. L. Lage, "Natural convection in an enclosure with disconnected and conducting solid blocks.," *International Journal of Heat and Mass Transfer*, vol. 48, no. 7, pp. 1361-1372, 2005.
- [55] Y. Feldman, *Direct Numerical Simulation of Transitions and Supercritical Regimes in Confined Three Dimensional Recirculating Flows*, the Zandman-Slander Graduate School of Engineering: Tel-Aviv University, Tel-Aviv, 2011.

תקציר

כיום, כמות בלתי מבוטלת של אנרגיה דרושה לצרכי מיזוג בנייני מגורים ומשרדים ואפילו מרכזי קניות. אופטימיזציה יעילה של תכונות הבידוד התרמי, עבור אבן בניין חלולה אשר נפוצה בתור חומר בניה בתעשייה, היא צעד חשוב בכיוון הגברת השליטה באקלים המקורה.

מטרת המחקר היא לפתח מתודולוגיה מוכללת עבור תכנון חומרים מבודדי-חום פאסיביים "חכמים" בהתבסס על הערכות סטטיסטיות של הזרימה התחומה עבור זורם המונע על ידי מנגנון הסעה טבעית בנוכחות חומר נקבובי. הסעה טבעית תחומה המתפתחת בתוך חלל המחומם באופן דיפרנציאלי (המהווה מודל נוח עבור חלל אוויר בליבת אבן הבניין החלולה) נבחרה בתור פלטפורמה עבור הסביבה החישובית.

החומר הנקבובי ההטרוגני מודל על ידי מצע גלילים צפופים שווי/שוני-גודל אשר לא מחוברים זה לזה. כל צילינדר ממוקם בצורה אינטליגנטית בתוך הזורם כך שיצור דיכוי יעיל של התנע בנקודות האנרגטיות ביותר עבור אותו זורם אשר מונע כתוצאה ממנגנון ההסעה הטבעית. מיקום מרכז כל גליל הושג על ידי יישום אנליזת יציבות ליניארית עבור הסעה טבעית דו-ממדית בנוכחות חומר נקבובי. התייחסות לזורם בגישת ה-mesoscale פותר באופן מפורש את שדה הזרימה בקרבת הגלילים השקועים על ידי גישת הגוף השקוע (IBM). התוצאות אוששו באופן נרחב עבור זרימה מציאותית תלת-ממדית.

בוצע ניתוח סטטיסטי בסיסי של תצורות החומרים הנקבוביים על מנת להכליל את הפיות של חומרים מבודדי-חום "חכמים". נמצא, כי יעילות מבודד החום המכיל חומר הנקבובי תלויה בקוטר הגלילים הנמצאים בתצורות החומר הנקבובי. המחקר קבע גישה מוכללת אשר מאפשרת תכנון וייצור חומרי בידוד-חום "חכמים" מחומרי "מדף" נקבוביים.



אוניברסיטת בן גוריון בנגד
הפקולטה למדעי ההנדסה
המחלקה להנדסת מכונות

חקירת הסעה טבעית בתוך תווך נקבובי על ידי שימוש בגישת הגוף השקוע (IBM)

על ידי: שחר עידן

אוקטובר 2016